The Company of Biologists

RESEARCH ARTICLE

Non-cell autonomous control of precerebellar neuron migration by Slit and Robo proteins

Chloé Dominici, Quentin Rappeneau, Pavol Zelina, Stéphane Fouquet and Alain Chédotal*

ABSTRACT

During development, precerebellar neurons migrate tangentially from the dorsal hindbrain to the floor plate. Their axons cross it but their cell bodies stop their ventral migration upon reaching the midline. It has previously been shown that Slit chemorepellents and their receptors, Robo1 and Robo2, might control the migration of precerebellar neurons in a repulsive manner. Here, we have used a conditional knockout strategy in mice to test this hypothesis. We show that the targeted inactivation of the expression of *Robo1* and *Robo2* receptors in precerebellar neurons does not perturb their migration and that they still stop at the midline. The selective ablation of the expression of all three Slit proteins in floor-plate cells has no effect on pontine neurons and only induces the migration of a small subset of inferior olivary neurons across the floor plate. Likewise, we show that the expression of Slit proteins in the facial nucleus is dispensable for pontine neuron migration. Together, these results show that Robo1 and Robo2 receptors act non-cell autonomously in migrating precerebellar neurons and that floor-plate signals, other than Slit proteins, must exist to prevent midline crossing.

KEY WORDS: Robo, Slit, Cerebellum, Floor plate, Inferior olive, Migration

INTRODUCTION

First described in human embryos (His, 1891), the rhombic lip, a germinative neuropithelium lining the dorsal edge of the fourth ventricle in the hindbrain, is the source of inferior olivary (IO) neurons and pontine (PN) neurons that both migrate tangentially, parallel to the pial surface, to the ventral midline or floor plate (Altman and Bayer, 1987; Essick, 1907, 1912; Harkmark, 1954). IO and PN neurons are precerebellar neurons that project into the contralateral cerebellum on Purkinje cells and granule cells, respectively. During their migration, they exhibit a unipolar morphology with a long leading process at the front (Bourrat and Sotelo, 1988; Kawauchi et al., 2006; Watanabe and Murakami, 2009; Zelina et al., 2014), which transform into an axon after midline crossing. However, PN neurons do not cross the midline, except for a few that are early born (Kawauchi et al., 2006). Insights onto the mechanisms controlling the migration of precerebellar neurons towards the midline have come from the phenotypic analysis of knockout mice. The current model suggests that precerebellar neuron guidance primarily relies on the same cues, netrin 1 (Ntn1) and Slit proteins (Slits) that control midline crossing

Sorbonne Universités, UPMC Paris 06, INSERM, CNRS, Institut de la Vision 75012, Paris, France.

*Author for correspondence (alain.chedotal@inserm.fr)

A.C., 0000-0001-7577-3794

of dorsal spinal cord commissural axons (Chédotal, 2011; Sotelo and Chédotal, 2013). In mice lacking Ntn1 or its receptor, deleted in colorectal carcinoma (Dcc), the ventral migration of IO and PN neurons is severely perturbed (Bloch-Gallego et al., 1999; Dominici et al., 2017; Marcos et al., 2009; Yee et al., 1999; Zelina et al., 2014). The abnormal dorsal expression of Ntn1 in the Ezh2 histone methyltransferase knockout induces a premature ventral migration on a subset of PN neurons (Di Meglio et al., 2013). Slit chemorepellents and their cognate receptors, roundabout 1 (Robo1) and Robo2 are also thought to influence precerebellar neuron migration. In both *Slit1;Slit2* and *Robo1;Robo2* double-knockout mice, a significant fraction of IO neurons crosses the floor plate (Di Meglio et al., 2008) and chains of PN neurons prematurely leave the main migratory stream, moving directly to the midline (Geisen et al., 2008). It has also been suggested that Slits released by the facial nucleus force PN neurons to migrate anteriorly before they can turn ventrally (Geisen et al., 2008) (see Fig. 2).

A third Robo receptor, Robo3, is expressed by precerebellar neurons until their leading processes cross the midline (Marillat et al., 2004; Zelina et al., 2014). In *Robo3* knockout (Marillat et al., 2004; Zelina et al., 2014) and in humans carrying mutations in *ROBO3* (Jen et al., 2004), PN neurons are unable to reach the ventral midline. IO neurons reach the floor plate but their axons fail to cross it (Marillat et al., 2004). Robo3 does not bind Slits in mammals and forms a complex with Dcc that promotes PN neuron ventral migration (Zelina et al., 2014). A partial rescue of the IO commissure in *Robo1/2/3* triple knockout suggests that Robo3 might counteract Slit/Robo repulsion, as proposed for spinal cord commissural axons (Di Meglio et al., 2008; Jaworski et al., 2010; Sabatier et al., 2004). Importantly, except for Robo3, the genetic data supporting the actual models come from phenotypic analysis of full knockouts in which Slits, Robo1 and Robo2 are inactivated in all cells. These molecules are broadly expressed throughout the body and the development of many neuronal systems and organs is severely impaired in *Slit1;Slit2* and *Robo1;Robo2* knockouts (Blockus and Chédotal, 2016; Ypsilanti et al., 2010). Therefore, direct genetic evidence validating the current working models could only be provided by a conditional knockout approach. Using this strategy, we show here that Slit/Robo signaling acts on precerebellar neurons in a non-cell-autonomous manner.

RESULTS

To study the role of Slits and Robo receptors in the migration of IO and PN neurons, we used and combined existing knockout lines, including *Slit2* (Rama et al., 2015) and *Robo2* (Gibson et al., 2014) conditional knockouts (*Slit2^{L/L}* and *Robo2^{L/L}*; see Materials and methods). *Slit2^{L/L}* mice were crossed to *Slit1* (Plump et al., 2002) and *Slit3* (Yuan et al., 2003) full knockouts and *Robo2^{L/L}* mice were intercrossed with *Robo1* knockouts (Gibson et al., 2014).

DEVELOPMENT
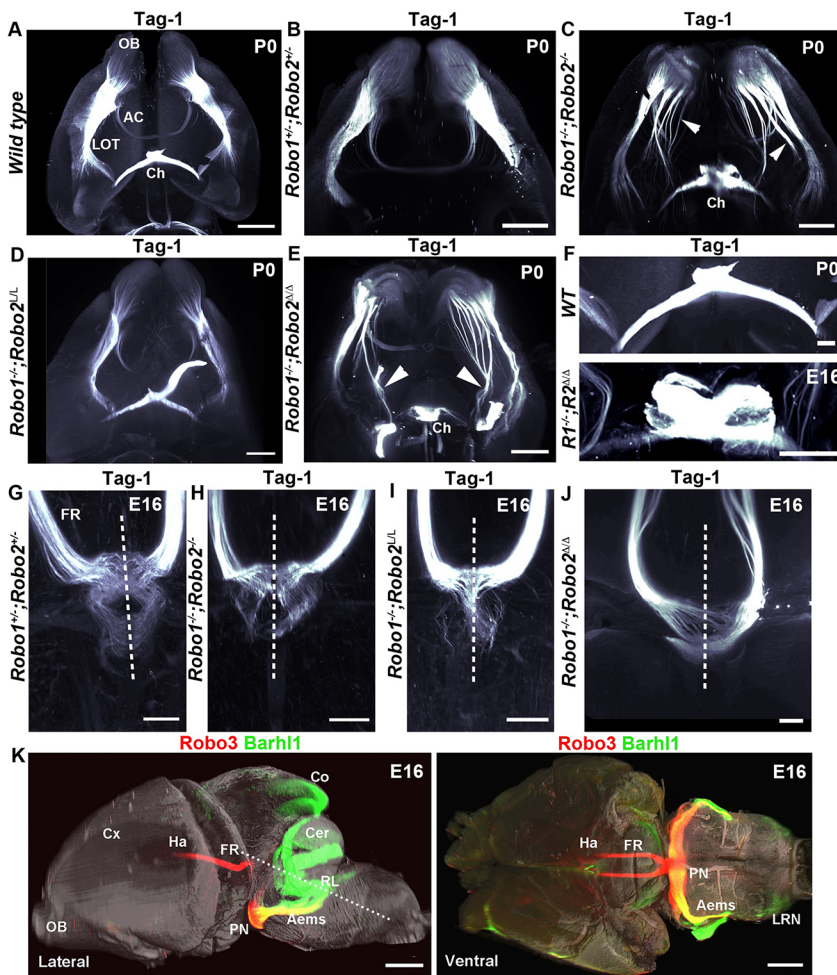
Fig. 1. $Robo1^{-/-};Robo2^{\Delta/\Delta}$ mice phenocopy $Robo1^{-/-};Robo2^{-/-}$ knockouts. (A-E) LSFM images (ventral views) of the forebrain. Tag-1 immunostaining and 3DISCO clearing. The LOT is defasciculated (arrowheads) and closer to the midline in $Robo1^{-/-};Robo2^{-/-}$ (C) and $Robo1^{-/-};Robo2^{\Delta/\Delta}$ (E) mice compared with controls (A,B,D). (F) The chiasm (Ch) is also disorganized in $Robo1^{-/-};Robo2^{\Delta/\Delta}$ mutants. (G-J) Tag1$^+$ axons from the fasciculus retroflexus (FR) cross the floor plate (dashed line) multiple times in $Robo1^{+/-};Robo2^{+/-}$ embryos (G) but not in $Robo1^{-/-};Robo2^{-/-}$ (H), $Robo1^{-/-};Robo2^{L/L}$ (I) and $Robo1^{-/-};Robo2^{\Delta/\Delta}$ (J) mutants. (K) LSFM views (lateral and ventral) of 3DISCO-cleared E16 brains immunostained for Robo3 (red) and Barhl1 (green). AC, anterior commissure; Aems, anterior extramural stream; Cer, cerebellum; Ch, chiasm; Co, colliculus; Cx, cortex; FR, fasciculus retroflexus; Ha, habenula; LRN, lateral reticular nucleus; OB, olfactory bulb; PN, pons; RL, rhombic lip. Scale bars: 1 mm in A; 400 μm in B,D; 300 μm in C,E,H; 200 μm in F,G,I,J; 800 μm in K.

Non-cell-autonomous control of pontine neuron migration by Robo1 and Robo2 receptors

To assess the role of Robo1 and Robo2 receptors in precerebellar neuron migration, we first intercrossed $Robo1^{-/-};Robo2^{L/L}$ and $Krox20:Cre$ mice, which express Cre recombinase in the germline (Voiculescu et al., 2000). The resulting homozygous mutants will be referred to as $Robo1^{-/-};Robo2^{\Delta/\Delta}$. Cre is also expressed in rhombomeres 3 and 5, which do not contain PN neuron progenitors (Di Meglio et al., 2013). In E13 hindbrain, Robo1 and Robo2 antibodies labeled longitudinal axons (Fig. S1B,E). The absence of $Robo2$ mRNA and protein in $Robo1^{-/-};Robo2^{\Delta/\Delta}$ embryos was confirmed by *in situ* hybridization and immunostaining (Fig. S1A-D). The lateral olfactory tract (LOT), which contains axons projecting from the olfactory bulb to the pyriform cortex is defasciculated in $Robo1/Robo2$ double knockouts (Fouquet et al., 2007). In those mutants, severe axon pathfinding defects were also described for the fasciculus retroflexus (FR), which connect the medial habenula to the interpeduncular nucleus (Belle et al., 2014). To visualize the LOT and FR in the various lines, we performed whole-mount immunolabeling with antibodies against transient-associated glycoprotein 1 (Tag-1/contactin 2) (Belle et al., 2014; Wolfer et al., 1994), combined with 3DISCO tissue clearing and light-sheet fluorescence microscopy (LSFM) (Belle et al., 2014). In E16 and P0 control brains from wild type (n=3/3), $Robo1^{+/-};Robo2^{+/-}$ (n=3/3), $Robo1^{+/-};Robo2^{L/+}$ (n=3/3) and $Robo1^{-/-};Robo^{L/L}$ (n=5/5) mice, Tag-1$^+$ LOT axons form one axon bundle extending on each side of the ventral forebrain (Fig. 1 and not

shown). In $Robo1^{-/-};Robo2^{-/-}$ (Fig. 1C; n=4/4) and $Robo1^{-/-};Robo2^{\Delta/\Delta}$ mice (Fig. 1E; n=8/8), the LOT was defasciculated and some axons extended more medially than in controls. As shown before in $Robo1^{-/-};Robo2^{-/-}$ knockouts (Plachez et al., 2008), midline crossing was abnormal at the optic chiasm of all $Robo1^{-/-};Robo2^{\Delta/\Delta}$ mutants (Fig. 1F). In wild type (n=3/3), $Robo1^{+/-};Robo2^{+/-}$ (n=3/3) and $Robo1^{+/-};Robo2^{L/+}$ (n=3/3), FR axons zigzagged at the floor plate upon reaching it (Fig. 1G). In $Robo1^{-/-};Robo^{L/L}$ (n=4/4), midline crossing was perturbed and some axons remained at the floor plate (Fig. 1I). In $Robo1^{-/-};Robo2^{-/-}$ (n=3/3) and $Robo1^{-/-};Robo2^{\Delta/\Delta}$ (n=3/3) mice, FR axon crossing was more strongly affected and most axons remained on the ipsilateral side (Fig. 1H,J; Belle et al., 2014). These results show that $Robo1^{-/-};Robo2^{\Delta/\Delta}$ mice phenocopy $Robo1^{-/-};Robo2^{-/-}$ double knockouts (Fig. 1F).

To study PN neuron migration, whole-mount double immunostaining for Robo3 and the transcription factor Barhl1 (Zelina et al., 2014) was performed on whole E16 embryos. This was also followed by 3DISCO clearing and LSFM (Fig. 1K; see Materials and methods). In all E16 wild-type (n=3/3), $Robo1^{+/-};Robo2^{+/-}$ (n=3/3), $Robo1^{+/-};Robo2^{L/+}$ (n=3/3) and $Robo1^{-/-};Robo^{L/L}$ (n=4/4) embryos (Fig. 2A,C,E; Movie 1 and not shown), PN neurons form a compact stream that migrates rostrally and then ventrally to the floor plate. They strongly express Barhl1 and Robo3. At this stage, Robo3 is also expressed in the FR, which terminates in the interpeduncular nucleus, rostral to the PN. As previously described (Geisen et al., 2008), PN migration was severely
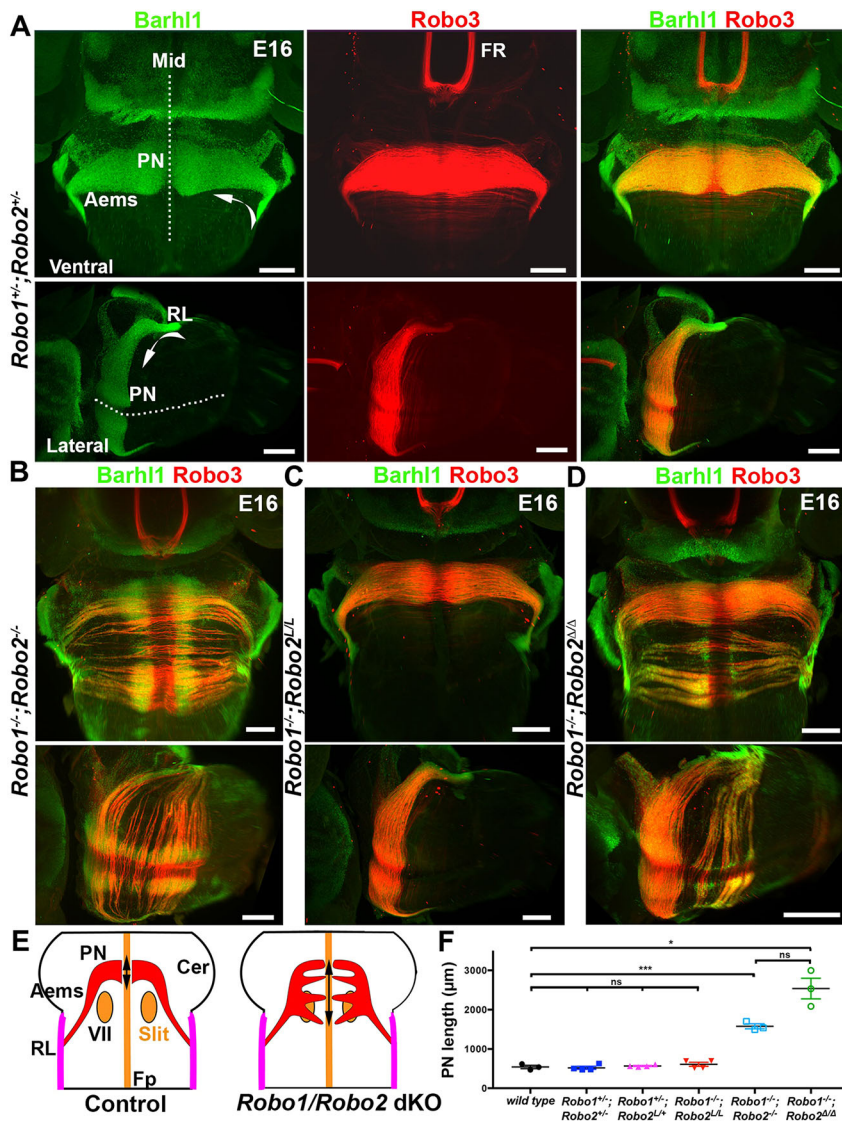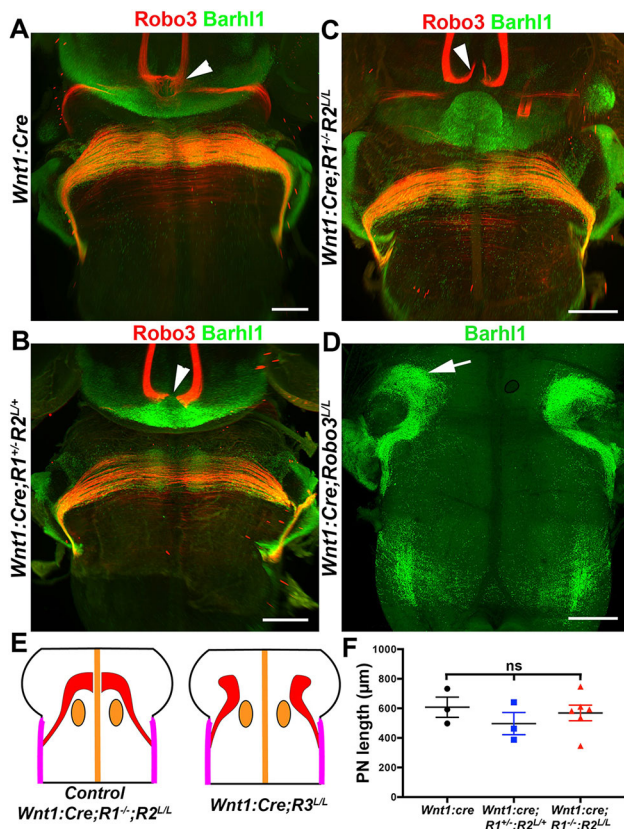
Fig. 2. PN neurons migrate prematurely to the midline in _Robo1⁻/⁻;Robo2^{Δ/Δ}_ mice. (A-D) LSFM images of 3DISCO-cleared E16 hindbrains immunostained for Barhl1 and Robo3. (A) Ventral views (top panels) and lateral views of a _Robo1^{+/−};Robo2^{+/−}_ embryo illustrating the normal migration pathway (Aems and curved arrow) followed by PN neurons from the rhombic lip to the midline (dashed line). (B,C) Many PN neurons migrate prematurely to the midline in _Robo1^{−/−};Robo2^{−/−}_ knockouts (B), unlike in _Robo1^{−/−};Robo2^{L/L}_ embryos (C). (D) _Robo1^{−/−};Robo2^{Δ/Δ}_ embryos phenocopy _Robo1^{−/−};Robo2^{−/−}_ mutants. (E) Schematic representations of PN neuron migration (red) in controls and Robo mutants. The black arrows indicate the PN length measured in F. Slits are found in the floor plate and facial nuclei (VII). (F) Quantification of PN length in Robo1/Robo2 mutants. *$P<0.05$, ***$P<0.001$. ns, not significant (_Robo1^{+/−};Robo2^{+/−}_, $P=0.7243$; _Robo1^{+/−};Robo2^{L/+}_, $P=0.6165$; _Robo1^{−/−};Robo2^{L/L}_, $P=0.3592$; Welch's _t_-test). Error bars indicate s.e.m. Aems, anterior extramural stream; Cer, cerebellum; Fp, floor plate; FR, fasciculus retroflexus; Mid, midbrain; PN, pontine; RL, rhombic lip. Scale bars: 400 µm in A-D (top panels); 500 µm in A-D (bottom panels).

perturbed in _Robo1^{−/−};Robo2^{−/−}_ ($n=3/3$; Fig. 2B; Movie 2) embryos, and multiple chains of Barhl1⁺/Robo3⁺ neurons left the normal pathway to prematurely migrate towards the floor plate. However, in _Robo1^{−/−};Robo2^{−/−}_ mutants, as in controls, Barhl1⁺ PN neurons aggregated on both sides of the floor plate without penetrating it, whereas their axons labeled with Robo3 crossed it. The quantification of the spreading of PN neurons along the floor plate supported the severe defasciculation of migrating PN neurons in _Robo1^{−/−};Robo2^{−/−}_ mutants (Fig. 2E,F). PN migration defects were strikingly similar in _Robo1^{−/−};Robo2^{Δ/Δ}_ embryos ($n=3/3$; Fig. 2D-F; Movie 3), further validating the _Robo2^{L/L}_ conditional knockout line. To determine whether Robo1/Robo2 act cell-autonomously in migrating PN neurons, we next intercrossed _Robo1^{−/−};Robo2^{L/L}_ mice and _Wnt1:Cre_ mice, which are known to drive the expression of Cre recombinase in PN neuron precursors in addition to other hindbrain neurons and neural crest cell derivatives (Di Meglio et al., 2013; Nichols and Bruce, 2006; Rodriguez and Dymecki, 2000; Zelina et al., 2014). In _Wnt1:Cre_ E16 embryos ($n=3/3$) and _Wnt1:Cre;Robo1^{+/−};Robo2^{L/+}_ ($n=3/3$) embryos, all Robo3⁺/Barhl1⁺ PN neurons migrated to the floor plate as in wild-type embryos, but the shape of the PN nucleus appeared slightly reduced and some FR axons failed to cross the midline (Fig. 3A,B).

Surprisingly, the migration of PN neurons was not affected in any of the _Wnt1:Cre;Robo1^{−/−};Robo2^{L/L}_ ($n=6/6$) embryos, in which all neurons followed the anterior extramural stream. No evidence of a premature migration to the ventral midline was found and PN length was similar to control (Fig. 3C,E,F). By contrast, all PN neurons failed to reach the midline in _Wnt1:Cre;Robo3^{L/L}_ embryos (Fig. 3D, E; $n=3/3$), thereby confirming that the _Wnt1:Cre_ line efficiently recombines floxed alleles in PN neuron precursors. Although Robo2 mRNA was previously detected in migrating pontine neurons (Geisen et al., 2008), unilateral electroporation in PN neurons of a plasmid encoding GFP ($n=3$ wild-type embryos; see Materials and methods) showed that Robo2 immunoreactivity was detectable only on post-crossing pontine axons (Fig. S1F-I), confirming an earlier report. Together, these data show that Robo1 and Robo2 do not control the migration of PN neurons in a cell-autonomous manner.

Floor plate-derived Slits do not influence PN neuron migration

To study the influence of floor plate-derived Slits on the migration of PN neurons, we next generated _Shh:Cre;Slit1^{−/−};Slit2^{lox/lox};Slit3^{−/−}_ (hereafter referred to as _Shh:Cre;S1^{−/−};S2^{L/L};S3^{−/−}_).

Fig. 3. PN neurons migrate normally in *Wnt1:Cre;Robo1$^{-/-}$;Robo2$^{L/L}$* knockouts. (A-D) LSFM images of 3DISCO-cleared E16 hindbrains immunostained for Barhl1 and Robo3. (A-C) PN neuron migration is normal in *Wnt1:Cre* (A) and *Wnt1:Cre;Robo1$^{+/-}$;Robo2$^{L/+}$* (B). However, FR axons do not properly cross the floor plate (arrowheads). (C) PN migration is not perturbed in *Wnt1:Cre;Robo1$^{-/-}$;Robo2$^{L/L}$* embryos. FR axons do not cross the midline (arrowhead). (D) PN neurons fail to turn ventrally in *Wnt1:Cre; Robo3$^{L/L}$* embryos (arrow). (E) Schematic representations of PN neuron migration (red) in controls and *Wnt1:Cre;Robo* mutants. (F) Quantification of PN length. ns, not significant (*Wnt1:Cre;Robo1$^{+/-}$;Robo2$^{L/+}$*, P=0.3370; *Wnt1: Cre;Robo1$^{-/-}$;Robo2$^{L/L}$*, P=0.6744; Welch's *t*-test). Error bars indicate s.e.m. Scale bars: 300 μm in A; 500 μm in B,C; 600 μm in D.

The viability of *Shh:Cre;S1$^{-/-}$;S2$^{L/L}$* mice was comparable with controls but *Shh:Cre;S1$^{-/-}$;S2$^{L/L}$;S3$^{-/-}$* mice died shortly after birth. In *Shh:Cre* mice, Cre recombinase and the reporter green fluorescent protein (GFP) are inserted in the sonic hedgehog locus and are expressed in the floor plate (Harfe et al., 2004; Joksimovic et al., 2009), as seen in E11 spinal cord sections (Fig. 4A). We first wanted to confirm that this line recapitulated the axon guidance defects previously described in *Sli1/Slit2/Slit3* triple knockouts (Long et al., 2004). *In situ* hybridization on E12 spinal cord sections from *Shh:Cre;S1$^{-/-}$;S2$^{L/L}$;S3$^{-/-}$* embryos with riboprobes specific for *Slit1*, *Slit2* exon 8 (floxed in *Slit2^{lox}* mice) or *Slit3* showed that they were all deleted from the floor plate, whereas Slit2 persisted in motoneurons (*n*=4/4; Fig. 4B-E). By contrast, *Ntn1* mRNA was expressed at normal levels in the floor plate of *Shh:Cre;S1$^{-/-}$;S2$^{L/L}$; S3$^{-/-}$* embryos. Immunostaining for GFP and Alcam (a floor-plate marker) confirmed that the floor plate appeared normal in *Shh:Cre; S1$^{-/-}$;S2$^{L/L}$;S3$^{-/-}$* embryos (Fig. S1J-O). To visualize spinal cord commissural axons, we performed immunolabeling of *S1$^{-/-}$;S2$^{L/L}$; S3$^{-/-}$* (*n*=3), *S1$^{-/-}$;S2$^{L/L}$;S3$^{+/-}$* (*n*=4), *S1$^{+/-}$;S2$^{L/+}$;S3$^{+/-}$* (*n*=3) and *Shh:Cre;S1$^{-/-}$;S2$^{L/L}$;S3$^{-/-}$* (*n*=10) E11-E12 embryos using antibodies against Robo3, Dcc and Robo1 (Jaworski et al., 2010).

As previously described in *Slit1/Slit2/Slit3* conventional triple knockout embryos (Long et al., 2004), midline crossing of Robo3$^+$ spinal cord commissural axons was similar to controls in *S1$^{-/-}$; S2$^{L/L}$;S3$^{-/-}$* embryos (Fig. 4F), further pointing to the redundant activity of Slit1-Slit3 at the floor plate. In *Shh:Cre;S1$^{-/-}$;S2$^{L/L}$; S3$^{-/-}$*, Robo3$^+$ commissural axons reached the midline but crossing was perturbed: the commissure was thicker and axons seemed to project towards the ventricular zone (Fig. 4G and Fig. S1P). LSFM imaging confirmed that the density of commissural axons was increased at the floor plate. Similar observations were made using anti-Dcc antibodies, which also confirmed the thickening of the ventral commissure in *Shh:Cre; S1$^{-/-}$;S2$^{L/L}$;S3$^{-/-}$* embryos (*n*=3/3) compared with *S1$^{-/-}$;S2$^{L/L}$; S3$^{-/-}$* embryos (*n*=3) and *S1$^{+/-}$;S2$^{L/+}$;S3$^{+/-}$* (*n*=3; Fig. 4H,I). The best evidence for abnormal midline crossing came from Robo1 immunolabeling. As previously shown in wild-type embryos (Long et al., 2004), Robo1 was only expressed on post-crossing commissural axons that had started to grow longitudinally and Robo1 staining was absent at the floor plate (Fig. 4H; *n*=3/3). By contrast, Robo1-positive axons were present in the floor plate of *Shh:Cre;S1$^{-/-}$;S2$^{L/L}$;S3$^{-/-}$* embryos (Fig. 4I; *n*=8/8). Guidance defects were observed at all spinal cord levels. These results support the floor-plate-specific deletion of the three Slits in our mutants and also the importance of floor-plate-derived Slits for spinal cord commissural axon guidance.

To further validate this strategy, we next analyzed the consequence of germline recombination of *Slit2* exon 8 in *S1$^{-/-}$; S2$^{L/L}$;S3$^{-/-}$* mice (see Materials and methods). So far, the phenotype of *Slit1/Slit2/Slit3* triple knockouts had just been analyzed in the spinal cord (Long et al., 2004).

We first focused on the LOT and FR projections as they are known to be affected in *Slit1;Slit2* null mice (Belle et al., 2014; Nguyen-Ba-Charvet et al., 2002). In wild type (*n*=3/3), *S1$^{-/-}$* (*n*=4/4) and *S1$^{-/-}$; S2$^{L/L}$* (*n*=5/5) P0 mice and E16 embryos, the LOT was confined to the lateral part of the forebrain, as shown with anti-Tag-1 labeling (Fig. 5A and not shown). As shown previously (Nguyen-Ba-Charvet et al., 2002), the LOT was defasciculated and bundles of axons invaded a more medial domain of the ventral forebrain in *S1$^{-/-}$;S2$^{-/-}$* double knockouts (Fig. 5B; *n*=3/3). Similar LOT guidance defects were also seen in *S1$^{-/-}$;S2$^{Δ/Δ}$;S3$^{+/-}$* embryos (*n*=4/4; Fig. 5C). At the level of the FR, midline crossing defects were found in *S1$^{-/-}$;S2$^{-/-}$* double knockouts (*n*=3/3) but not in *S1$^{-/-}$;S3$^{-/-}$* (*n*=3/3) and *S1$^{-/-}$; S2$^{L/L}$;S3$^{-/-}$* embryos (*n*=4/4; Fig. 5D,E). We found that the FR completely failed to cross the floor plate in *S1$^{-/-}$;S2$^{Δ/Δ}$;S3$^{-/-}$* embryos (*n*=4/4; Fig. 5F). These results confirm that axon guidance defects observed after germline deletion of exon 8 in *Slit2$^{L/L}$* mice faithfully mimic what was previously found using conventional *Slit2* knockouts.

We next studied the migration of PN neurons in *Slit* conditional knockouts. As previously described (Geisen et al., 2008), PN neurons migrated as in wild type in *S1$^{+/-}$;S2$^{L/+}$* (*n*=3/3), *S1$^{-/-}$;S3$^{+/-}$* (*n*=4/4), *S1$^{-/-}$* (*n*=4/4) and *S1$^{-/-}$;S2$^{L/L}$;S3$^{-/-}$* E16 embryos (*n*=4/4; Fig. 5G and not shown), whereas PN neuron migration was disorganized in *S1$^{-/-}$;S2$^{-/-}$* embryos (*n*=3/3; Fig. 5H; Movie 4), in which PN neurons directly migrated from the rhombic lip to the floor plate, resulting in a significant caudal extension of Barhl1$^+$ PN neurons clustering along the floor plate (Fig. S1Q). A slight rostro-caudal enlargement was also detected in *S1$^{-/-}$;S3$^{-/-}$* embryos but no ectopic migratory chains (Fig. S1Q, *n*=3/3). The severity of the PN premature migration defects appeared similar in *S1$^{-/-}$;S2$^{-/-}$;S3$^{-/-}$* E16 embryos (*n*=2; Fig. 5I; Movie 5). Likewise, a major disorganization of the PN migratory stream was seen in both
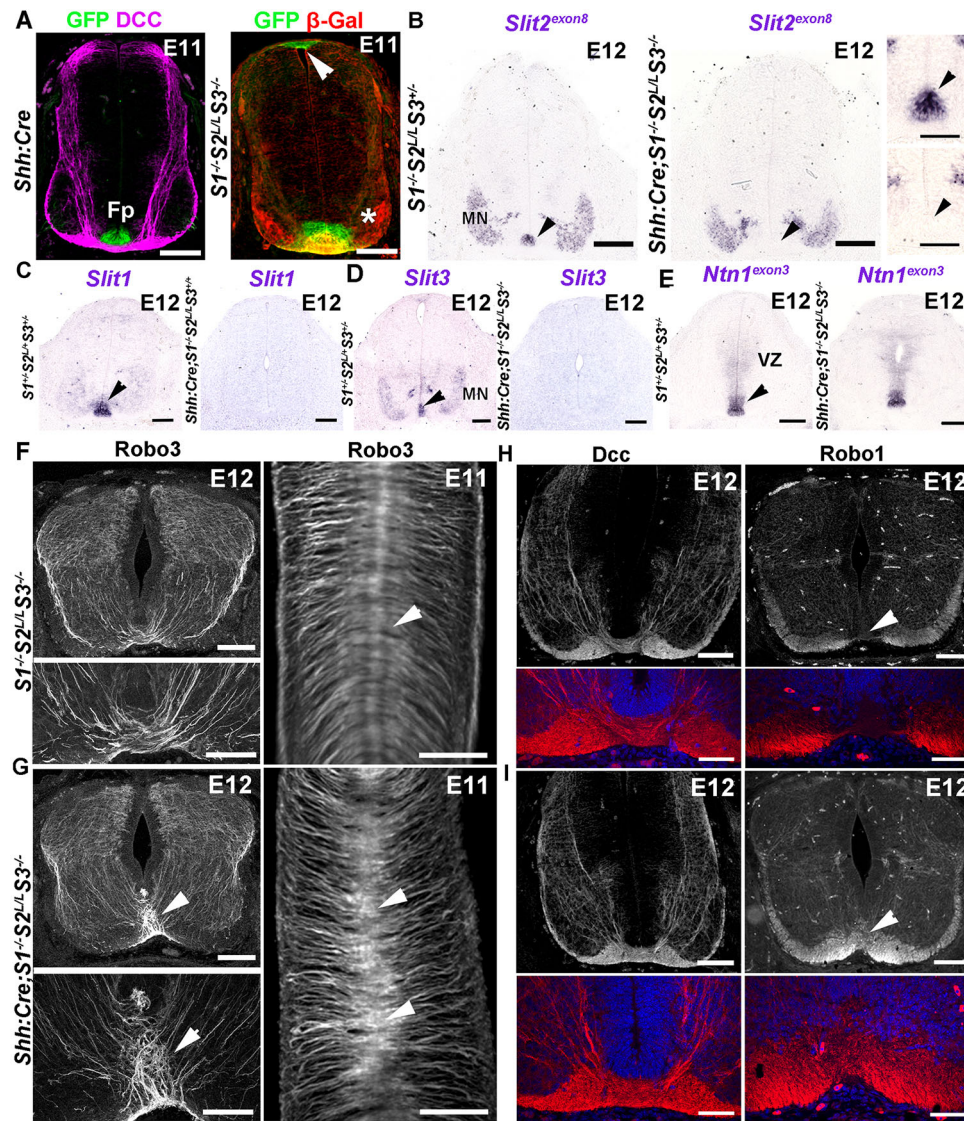
Fig. 4. Floor plate-derived Slits control midline crossing in the spinal cord. (A) Coronal sections of E11 *Shh:Cre* (left panel) and $S1^{-/-};S2^{L/L};S3^{-/-}$ (right panel) spinal cord immunolabeled for Dcc and GFP, or for β-galactosidase (β-gal) and GFP. In *Shh:Cre*, GFP is restricted to the floor plate (Fp) crossed by Dcc$^+$ commissural axons. In $S1^{-/-};S2^{L/L};S3^{-/-}$, GFP and β-gal are found in the floor plate. GFP is also in the roof plate (arrowhead) where *Slit1* is expressed (GFP was inserted in the *Slit1* locus in the *Slit1* knockout) and β-gal in motoneurons (asterisk). (B) Spinal cord sections of E12 $S1^{-/-};S2^{L/L};S3^{+/-}$ and *Shh:Cre;S1$^{-/-}$;S2$^{L/L}$;S3$^{-/-}$* embryos hybridized with a *Slit2* exon 8 riboprobe. In $S1^{-/-};S2^{L/L};S3^{-/-}$, *Slit2* is expressed at the floor plate (arrowhead) and in *Shh:Cre; S1$^{-/-}$;S2$^{L/L}$;S3$^{-/-}$*, *Slit2* is detected in motoneurons (MNs) but not in floor plate (arrowhead). Higher magnification views of the floor plate (arrowheads) are shown on the right. (C-E) E12 spinal cord sections. In $S1^{+/-};S2^{L/+};S3^{+/-}$, *Slit1*, *Slit3* and *Ntn1* mRNAs are in the floor plate (arrowhead). *Slit3* is also in motoneurons and *Ntn1* in the ventricular zone (VZ). In *Shh:Cre;S1$^{-/-}$;S2$^{L/L}$;S3$^{-/-}$*, *Slit1* and *Slit3* mRNAs are undetectable, whereas *Ntn1* expression is not affected. (F,G) Robo3 immunolabeling on E12 spinal cord sections (left panels) or on whole-mount E11 spinal cord (right panels; 3DISCO and LSFM). Robo3$^+$ axons accumulate at the floor plate (arrowheads in G) in *Shh:Cre;S1$^{-/-}$;S2$^{L/L}$;S3$^{-/-}$* embryos. Two longitudinal domains (arrowhead in F) with weaker Robo3 expression are absent in the *Shh:Cre;S1$^{-/-}$;S2$^{L/L}$;S3$^{-/-}$* mutant. (H,I) Confocal images of spinal cord sections from E12 embryos immunolabeled for Dcc (left panels) and Robo1 (right panels). The density of Dcc$^+$ axons at the floor plate is increased in *Shh:Cre;S1$^{-/-}$;S2$^{L/L}$;S3$^{-/-}$* mutant (I) compared with $S1^{-/-};S2^{L/L};S3^{-/-}$ (H). In $S1^{-/-};S2^{L/L};S3^{-/-}$ embryo, Robo1$^+$ axons are absent from floor plate (arrowhead in H) unlike in *Shh:Cre;S1$^{-/-}$;S2$^{L/L}$;S3$^{-/-}$* mutant (arrowhead in I). Scale bars: 100 μm in A-C,H,I; 50 μm in B (right panels); 150 μm in F,G.

$S1^{-/-};S2^{\Delta/\Delta};S3^{+/-}$ (n=6/6) and $S1^{-/-};S2^{\Delta/\Delta};S3^{-/-}$ mutants (n=5/5; Fig. 5K,L; Movie 6) with multiple chains of Barhl1$^+$/Robo3$^+$ neurons migrating ventrally, straight to the midline (Fig. S1Q). In addition, in both $S1^{-/-};S2^{\Delta/\Delta};S3^{-/-}$ mutants (n=5/5) and $S1^{-/-};S2^{-/-};S3^{-/-}$ E16 embryos (n=2/2) PN neurons invaded the floor plate, unlike in $S1^{-/-};S2^{-/-}$ embryos (Fig. 5J, n=3/3). As noted before (Geisen et al., 2008), migration defects were observed on both sides, but the right and left PN migratory streams were variably affected in all mutants (ectopic streams do

not always appear at the same positions, their number and width also differ), suggesting that loss of Slits partially randomizes PN neuron migration.

To determine whether the floor plate is an important source of Slits for migrating PN, we next studied hindbrain commissures and PN migration in *Shh:Cre;S1$^{-/-}$;S2$^{L/L}$;S3$^{-/-}$* mutants. GFP immunostaining confirmed that, as in the spinal cord, GFP is expressed by floor plate in the hindbrain of *Shh:Cre* embryos (Fig. 6A). *In situ* hybridization for *Slit2* exon 8 showed that *Slit2*
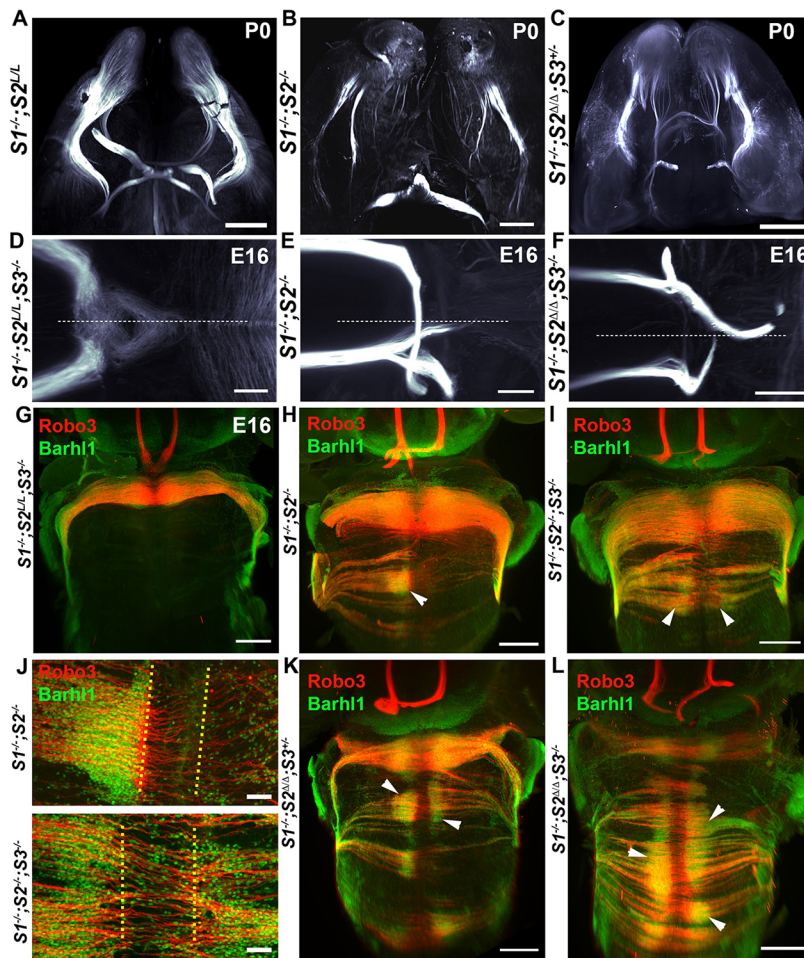
Fig. 5. Abnormal PN migration in *Slit1/Slit2/Slit3* triple knockouts. (A-F) LSFM images of 3DISCO-cleared E16 and P0 brains (ventral views) immunostained for Tag-1. In $S1^{-/-}$; $S2^{L/L}$ (A), the LOT is similar to controls, whereas in $S1^{-/-};S2^{-/-}$ (B) and $S1^{-/-};S2^{\Delta/\Delta};S3^{+/-}$ (C) embryos, LOT axons are defasciculated and project medially. (D-F) LSFM images illustrating FR axon midline (broken line) crossing defects in $S1^{-/-};S2^{-/-}$ and $S1^{-/-};S2^{\Delta/\Delta};S3^{-/-}$ mutant embryos. (G-L) LSFM images (G-I,K,L) and confocal images (J) of 3DISCO-cleared E16 embryo hindbrains immunolabeled for Barhl1 and Robo3. PN migration is normal in $S1^{-/-};S2^{L/L};S3^{-/-}$ (G). By contrast, in $S1^{-/-};S2^{-/-}$ (H), $S1^{-/-};S2^{-/-};S3^{-/-}$ (I), $S1^{-/-};S2^{\Delta/\Delta};S3^{+/-}$ (K) and $S1^{-/-};S2^{\Delta/\Delta};S3^{-/-}$ (L) mutants, multiple chains of PN neurons migrate directly from the rhombic lip to the floor plate, forming ectopic clusters (arrowheads). (J) Most ectopic PN neurons stop at the floor plate (between dotted lines) in $S1^{-/-};S2^{-/-}$ knockout (upper panel), whereas they enter it in great numbers in the $S1^{-/-};S2^{-/-};S3^{-/-}$ knockout (lower panel). Scale bars: 500 μm in A-C,G-I,K,L; 200 μm in D-F; 50 μm in J.

mRNA was deleted from the floor plate in *Shh:Cre;S1^{-/-};S2^{L/L};S3^{-/-}* (n=3) and *Shh:Cre;S1^{-/-};S2^{L/L}* (n=3) embryos, but that *Slit2* expression in the facial nuclei was as that in $S1^{-/-};S2^{L/L};S3^{+/-}$ embryos (n=3). To study hindbrain commissures, we first, performed immunostaining for Dcc, which showed that the thickness of hindbrain commissures was significantly increased at the floor plate in *Shh:Cre;S1^{-/-};S2^{L/L};S3^{-/-}* (n=3; Fig. 6C and Fig. S1R). As in the spinal cord, commissural axon midline crossing defects were best seen after Robo1 immunostaining. LSFM on 3DISCO-cleared E12 hindbrains showed that Robo1 labels longitudinal axons along the floor plate in $S1^{-/-};S2^{L/L};S3^{-/-}$ embryos (n=3/3), whereas aberrant crossing of Robo1⁺ axons was observed in *Shh:Cre;S1^{-/-};S2^{L/L};S3^{-/-}* mutants (n=3/3; Fig. 6D). Confocal imaging of hindbrain sections also showed this abnormal accumulation of Robo1⁺ axons at the floor plate of *Shh:Cre;S1^{-/-}; S2^{L/L};S3^{-/-}* embryos (n=3/3; Fig. 6D). Strikingly, we could not detect any PN migration defects in *Shh:Cre;S1^{-/-};S2^{L/L};S3^{+/-}* (n=4/4) or *Shh:Cre;S1^{-/-};S2^{L/L};S3^{-/-}* (n=4/4) mutants, and the shape and size of the PN migratory stream were comparable with *Shh:Cre;S1^{-/-};S2^{L/L};S3^{-/-}* controls: *Shh:cre,S1^{+/-};S2^{L/+}* (n=3), $S1^{+/-};S2^{L/+}$ (n=3/3), $S1^{-/-};S3^{-/-}$ (n=3/3), $S1^{-/-};S3^{+/-}$ (n=4/4), $S1^{-/-}$ (n=3/3) and $S1^{-/-};S2^{L/L};S3^{-/-}$ (n=3/3) (Fig. 6E and Fig. S1S; Movie 7). The abnormal midline crossing of FR axons in these embryos (Fig. 6F) confirmed that *Slit2* was efficiently inactivated in *Shh:Cre;S1^{-/-};S2^{L/L};S3^{-/-}* mice. Together, the lack of PN migration defects reveals that floor-plate-derived Slits do not play an important role in PN neuron migration.

Neurons in the facial nucleus express Slit2 and Slit3 (Geisen et al., 2008), and it was proposed that this is a main source of chemorepellents for PN neurons, during their longitudinal migration along the hindbrain. To test this hypothesis, we generated *Phox2b:Cre;S1^{-/-};S2^{L/L}* and *Phox2b:Cre;S1^{-/-};S2^{L/L}; S3^{-/-}* mice. Phox2b is a transcription factor that controls the specification of the facial motor nucleus (Pattyn et al., 2000). The expression of Cre recombinase in embryonic facial neurons was first validated by crossing *Phox2b:Cre* and *Tau^{GFP}* mice in which a membrane-tethered GFP is expressed in axons in the presence of Cre (Hippenmeyer et al., 2005) (Fig. 7A). *In situ* hybridization with a *Slit2* exon 8 probe on E12 *Phox2b:Cre;S1^{-/-};S2^{L/L}* (n=3/3) and *Phox2b:Cre;S1^{-/-};S2^{L/L};S3^{-/-}* mutants (n=3/3) showed that, unlike in $S1^{-/-};S2^{L/L}$ embryos (n=3/3), *Slit2* expression was prevented in the facial nucleus but maintained in the floor plate (Fig. 7B). The lack of Slit2 did not perturb the development of the facial nucleus, which had a similar position and morphology to that in *Phox2b:Cre; S1^{-/-};S2^{L/L};S3^{-/-}* mutants (n=3/3) and $S1^{-/-};S2^{L/L}$ embryos (n=3/3). Next, we analyzed the migration of PN neurons using Barhl1/Robo3 double immunolabeling and LSFM. We could not detect any PN migration defects in $S1^{-/-};S2^{L/L};S3^{-/-}$ (n=3/3), *Phox2b:Cre;S1^{-/-}; S2^{L/L}* (n=3/3) and *Phox2b:Cre;S1^{-/-};S2^{L/L};S3^{-/-}* (n=3/3) embryos (Fig. 7D-F and Fig. S2A; Movie 8). These results show that PN neurons migrate normally in the absence of Slit2 and Slit3 in the facial nucleus.

To determine whether the simultaneous inactivation of Slit1-Slit3 at the level of the floor plate and facial nucleus perturbs PN neuron
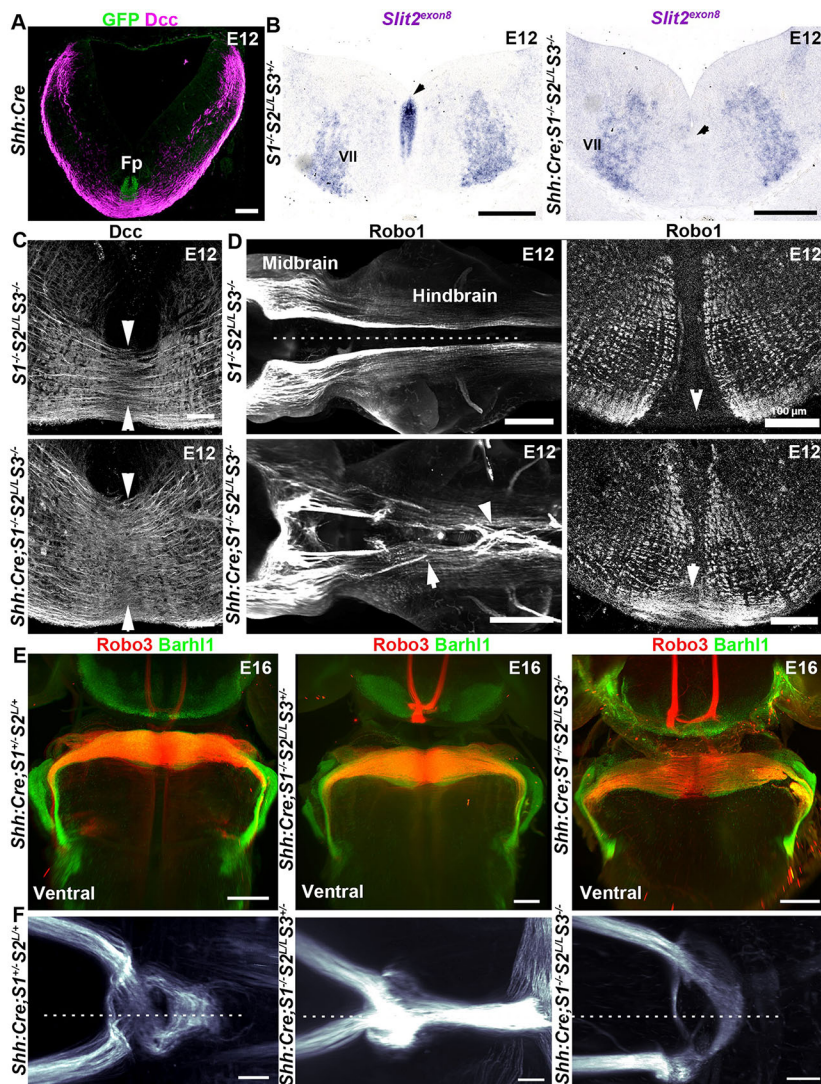
Fig. 6. Normal PN migration in *Shh:Cre;S1⁻/⁻;S2^{L/L};S3⁻/⁻* mutants. (A) Coronal sections of an E12 *Shh:Cre* embryo immunolabeled for Dcc and GFP. GFP⁺ floor plate (Fp) is crossed by Dcc⁺ commissural axons. (B) *In situ* hybridization with a *Slit2* exon 8 probe on E12 coronal sections at the level of the facial nucleus (VII) of *S1⁻/⁻;S2^{L/L};S3⁺/⁻* (left) and *Shh:Cre;S1⁻/⁻;S2^{L/L};S3⁻/⁻* (right) embryos. Slit2 is absent from Fp in the *Shh:Cre;S1⁻/⁻;S2^{L/L};S3⁻/⁻* embryo (arrowheads), but still present in facial nuclei. (C) Confocal images of E12 hindbrain commissures labeled using anti-Dcc antibody. The commissure (between arrowheads) is enlarged in *Shh:Cre; S1⁻/⁻;S2^{L/L};S3⁻/⁻* (bottom panel) compared with *S1⁻/⁻; S2^{L/L};S3⁻/⁻*. (D) LSFM (left panels) and confocal (right panels) images of *S1⁻/⁻;S2^{L/L};S3⁻/⁻* (upper panels) and *Shh:Cre;S1⁻/⁻;S2^{L/L};S3⁻/⁻* (lower panels) embryos immunolabeled for Robo1. In *Shh:Cre;S1⁻/⁻;S2^{L/L};S3⁻/⁻* mutants, longitudinal Robo1⁺ axons extending from the midbrain to the hindbrain abnormally enter the midline (arrowheads). (E,F) LSFM images (ventral views) of E16 hindbrain after Barhl1/Robo3 immunostaining. PN migration is similar in *Shh:Cre;S1⁺/⁻;S2^{L/+};S3⁺/⁻* controls and in *Shh: Cre;S1⁻/⁻;S2^{L/L};S3⁺/⁻* or *Shh:Cre;S1⁻/⁻;S2^{L/L};S3⁻/⁻* mutants (E). By contrast, severe FR axon midline crossing defects exist in *Shh:Cre;S1⁻/⁻;S2^{L/L};S3⁺/⁻* and *Shh:Cre;S1⁻/⁻;S2^{L/L}; S3⁻/⁻* mutants (F). Scale bars: 100 μm in A,C,D (right panels); 250 μm in B; 400 μm in D (left panels); 500 μm in E; 200 μm in F.

migration, we generated E16 *Shh:Cre;Phox2b:Cre;S1⁻/⁻;S2^{L/L}; S3⁻/⁻*. Interestingly, a few streams of ectopic and prematurely migrating PN neurons were found in *Shh:Cre;Phox2b:Cre;S1⁻/⁻; S2^{L/L};S3⁺/⁻* embryos (*n*=3/3; Fig. 7G) and in *Shh:Cre;Phox2b:Cre; S1⁻/⁻;S2^{L/L};S3⁻/⁻* embryos (*n*=2/3; Fig. 7H; Movie 9). Confocal imaging of the ectopic PN clusters showed axons crossing the midline but also extending within the floor plate (Fig. 7I,J). Although minor PN migratory defects exist in mice simultaneously depleted of Slits in the floor plate and facial nucleus, the phenotype is much milder than after ubiquitous inactivation of all Slits (Fig. 7K).

Revisiting the role of Slit/Robo signaling in IO development

The IO nucleus, does not develop properly in *Robo1/Robo2* and *Slit1/Slit2* double knockouts (Di Meglio et al., 2008; Geisen et al., 2008). To study the 3D organization of the IO nucleus in Slit and Robo conditional knockouts, we performed whole-mount immunostaining for Foxp2 (Fujita and Sugihara, 2012) followed by 3DISCO clearing and LSFM (Figs 8 and 9). The IO is adjacent to the floor plate and comprises several subnuclei organized in a lamellated pattern (Azizi and Woodward, 1987) (Fig. 8A,B). At P0, the 3D structure of the IO was comparable with wild type in *Robo1⁺/⁻;Robo2⁺/⁻* mice (*n*=3/3; Fig. 8C), whereas in *Robo1⁻/⁻;

Robo2⁻/⁻* (*n*=3/3; Fig. 8D) and *Robo1⁻/⁻;Robo2^{Δ/Δ}* mice (*n*=3/3; Fig. 8E), the IO was elongated and more compact. The circumferential migration of IO neurons starts around E11 and finishes by E14-E15 (Di Meglio et al., 2008). Optical sectioning with Imaris (see Materials and methods) was used to visualize migrating IO neurons at E13 (Fig. 8F; Movies 10-13). In wild type, Foxp2⁺ IO neurons stopped at the midline, whereas in *Robo1⁻/⁻; Robo2⁻/⁻* double knockouts and *Robo1⁻/⁻;Robo2^{Δ/Δ}* mice, a significant fraction of IO neurons migrated into the floor plate (*n*=3/3; Fig. S2B). Unilateral DiI injection into the cerebellum resulted in bilateral retrograde labeling of IO neurons in both *Robo1⁻/⁻;Robo2⁻/⁻* and *Robo1⁻/⁻;Robo2^{Δ/Δ}* mutants, whereas in wild type, labeled neurons are only contralateral (*n*=3/3 for each genotype; Figs 8G and 9I). To assess the cell-autonomous function of Robo1/2 receptors in IO neuron migration, we crossed the *Robo1⁻/⁻;Robo2^{L/L}* mice to the *Pft1a:Cre* line. Ptf1a is a transcription factor expressed by IO progenitors and the *Ptf1a:Cre* line drives Cre expression in IO neurons (Badura et al., 2013; Renier et al., 2010). *Pft1a:Cre;Robo1⁻/⁻;Robo2^{L/L}* mice were fully viable and did not exhibit any obvious motor deficits, unlike other IO mutants (Badura et al., 2013; Renier et al., 2010). At E12, the downregulation of Robo2 expression in a large fraction of hindbrain neurons was confirmed by immunostaining and *in situ* hybridization
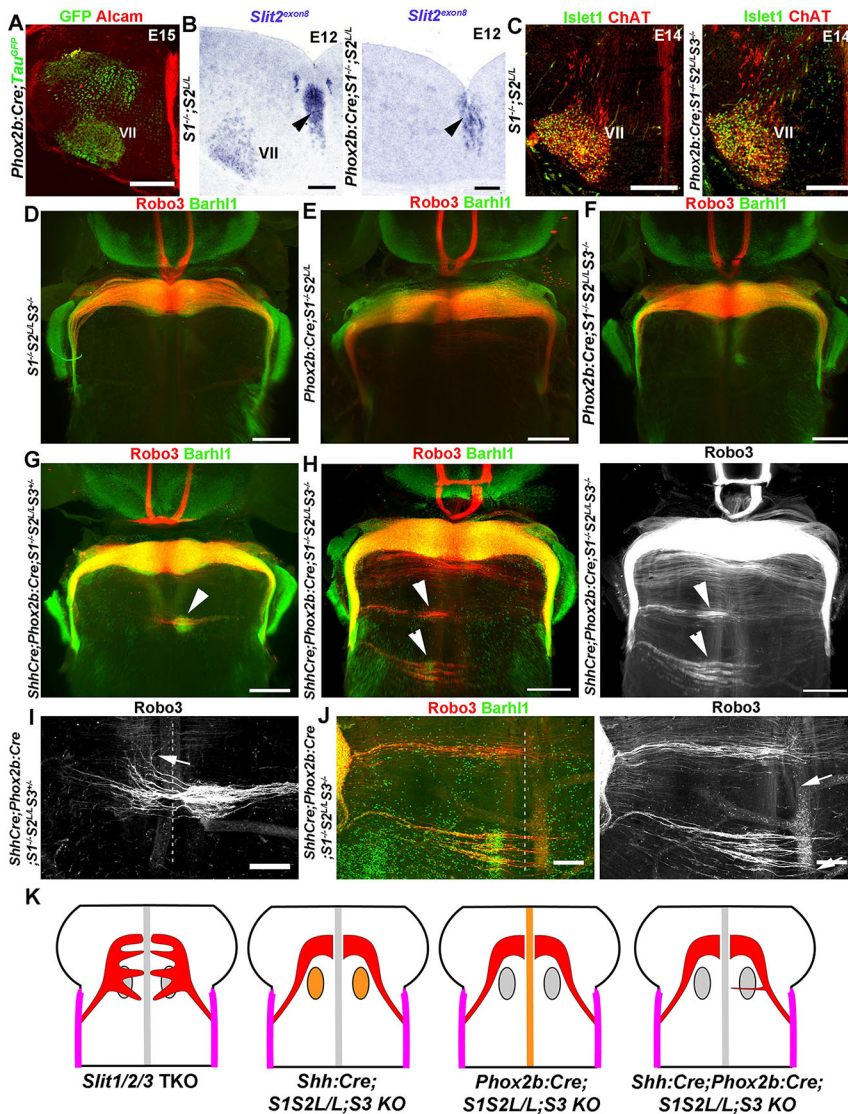
Fig. 7. PN migration in absence of Slit expression in the facial nucleus. (A) Coronal section at the level of the facial nucleus (VII) in a *Phox2b:Cre;Tau^GFP* E15 embryo immunolabeled for GFP and Alcam, a motoneuron and floor-plate marker (Weiner et al., 2004). GFP is highly expressed in facial nuclei (VII). (B) E12 coronal sections of *S1^−/−;S2^L/L* (left) and *Phox2b:Cre;S1^−/−;S2^L/L;S3^−/−* (right) embryos hybridized with a *Slit2* exon 8 probe. *Slit2* is in the floor plate (arrowheads), but absent from the VII nucleus in *Phox2b:Cre;S1^−/−;S2^L/L;S3^−/−* mutants. (C) Coronal sections of E12 *S1^−/−;S2^L/L* (left) and *Phox2b:Cre;S1^−/−;S2^L/L;S3^−/−* (right) embryos immunolabeled for the two motoneuron markers ChAT and islet 1. The VII nucleus labeling is similar. (D-H) LSFM images of E16 hindbrains labeled with Barhl1 and Robo3. The PN migration pathway is as in controls in *S1^−/−;S2^L/L;S3^−/−* (D), *Phox2b:Cre;S1^−/−;S2^L/L* (E) and *Phox2b:Cre;S1^−/−;S2^L/L;S3^−/−* (F) mutants. A few small streams of PN neurons (arrowheads) migrate prematurely to the midline in *Shh:Cre;Phox2b:Cre;S1^−/−;S2^L/L;S3^+/−* (G) and *Shh:Cre;Phox2b:Cre;S1^−/−;S2^L/L;S3^+/−* (H) mutants. (I,J) Confocal images of ectopic PN clusters. Some Robo3^+ PN axons extend along the floor plate (arrows). (K) Schematic representations of PN neuron migration (red) in *Slit* mutants. Scale bars: 250 μm in A; 100 μm in B; 150 μm in C,I,J; 500 μm in D-H.

(Fig. S2C,D). At P0, the shape of the IO in *Pft1a:Cre;Robo1^−/−; Robo2^L/L* mice was similar to controls (*n*=4/4; Fig. 8H) and IO neurons projected to the contralateral cerebellum (*n*=5/5; Fig. 8H). In P15 and adult *Pft1a:Cre;Robo1^−/−;Robo2^L/L* mice, the lamellation of the IO nucleus was also normal (*n*=3/3; Fig. 8I and not shown). These data suggest that the migration of IO neurons does not require Robo1/Robo2 receptors.

We next analyzed the role of floor-plate-derived Slits. At P0, LSFM confirmed that the IO shape was abnormal in *S1^−/−;S2^−/−* double knockouts (*n*=3/3; Fig. 9A; Di Meglio et al., 2008) with a lateromedial compaction similar to *Robo1/Robo2* knockouts. This was also the case in *S1^−/−;S2^Δ/Δ;S3^+/−* mice (*n*=3/3) but not in *S1^−/−;S2^L/L;S3^+/−* (*n*=5/5), *S1^−/−;S2^L/L* (*n*=3/3), *S1^−/−;S3^−/−* (*n*=3/3) or *S1^−/−* (*n*=3/3) mice (Fig. 9B,C). In *Shh:Cre;S1^−/−; S2^L/L;S3^−/−* (*n*=3/3) and *Shh:Cre;S1^−/−;S2^L/L* mice (*n*=3/3), the overall IO shape was similar to controls, but gaps devoid of Foxp2 IO neurons could be seen (Fig. 9D). DiI-labeled IO neurons were contralateral in *S1^−/−;S2^L/L* (*n*=4/4) and *S1^−/−; S2^L/L;S3^−/−* (*n*=3/3) newborn mice (Fig. 9E,I). By contrast, DiI-labeled neurons were also observed ipsilaterally in *Shh:Cre;S1^−/−;S2^L/L;S3^+/−* embryos (*n*=4/4) and to a larger extent in *Shh:Cre;S1^−/−;S2^L/L;S3^−/−* mutants (*n*=3/3), suggesting that some neurons might have crossed the floor

plate. Accordingly, Foxp2+IO neurons were observed in the floor plate of *S1^−/−;S2^−/−* (*n*=3/3), *S1^−/−;S2^Δ/Δ;S3^+/−* (*n*=3/3) and *S1^−/−; S2^Δ/Δ;S3^−/−* (*n*=4/4) E13 embryos, as well as in E14 *Shh:Cre;S1^−/−; S2^L/L;S3^+/−* (*n*=3/3) and *Shh:Cre;S1^−/−;S2^L/L;S3^−/−* (*n*=3/3) embryos but not in *S1^−/−;S2^L/L* embryos (*n*=3/3) and *S1^−/−;S2^L/L; S3^−/−* (*n*=4/4) (Fig. 9F,G). The abnormal morphology of the IO complex in *Shh:Cre;S1^−/−; S2^L/L* was still observed in P25 and adult animals (*n*=4/4; Fig. 9H and not shown), indicating that lamellation defects were not corrected after birth.

DISCUSSION
Robo receptors were discovered because of their role in commissural axon guidance in the *Drosophila* nerve cord (Kidd et al., 1998; Seeger et al., 1993). *Drosophila* Robo receptors (Robos) bind Slit and trigger a repulsive signal (Kidd et al., 1999). This function of Slits and Robos in the regulation of midline crossing seems to be conserved across evolution from worm to humans (Brose et al., 1999; Fricke et al., 2001; Jen et al., 2004; Zallen et al., 1999). In rodents, genetic evidence supporting a repulsive activity of Slit/Robo signaling for commissural axons has been obtained in various neuronal systems through the phenotypic analysis of Slit and Robo knockout mice (Bagri et al., 2002; Fouquet
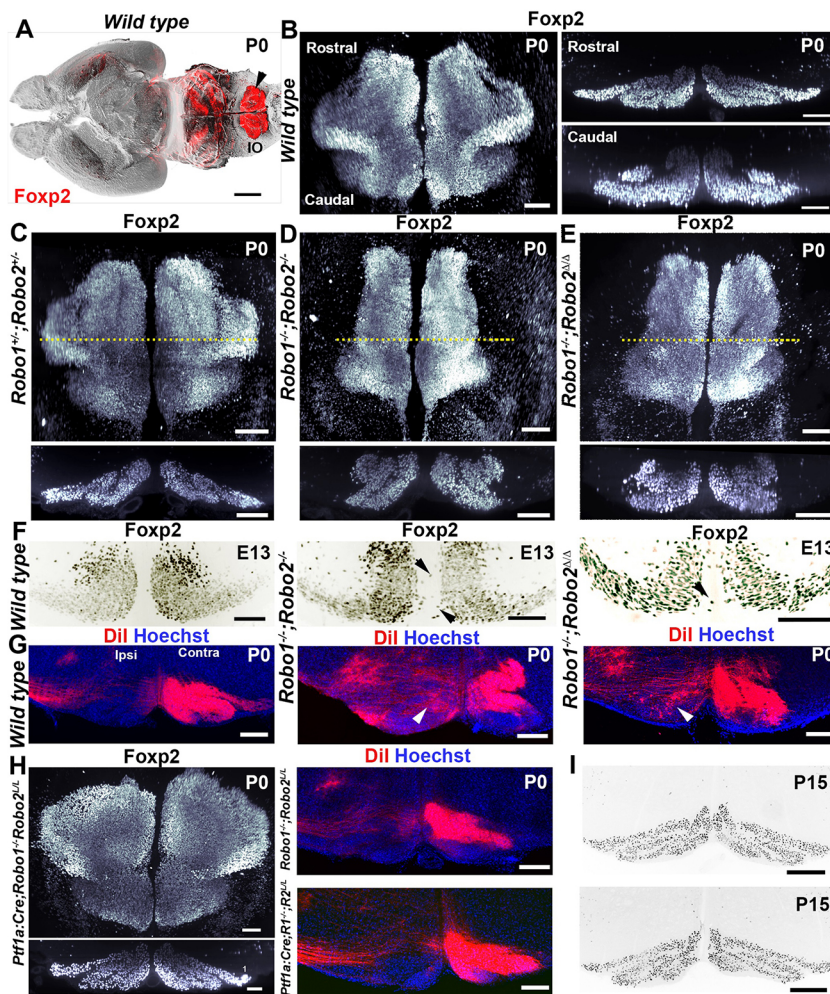
Fig. 8. Robo1/2 receptors do not control cell-autonomous midline crossing of IO neurons. (A) LSFM image (ventral view) of a wild-type P0 brain immunolabeled for Foxp2. The inferior olive (IO, arrowhead) strongly expresses Foxp2. (B) High magnification of the IO (left) and optical sections (right) illustrating IO lamellation. (C-E) LSFM images the IO in *Robo1⁺/⁻;Robo2⁺/⁻* (C), *Robo1⁻/⁻;Robo2⁻/⁻* (D) and *Robo1⁻/⁻;Robo2^{Δ/Δ}* (E) mice. IO morphology is abnormal and more compact in mice deficient for Robo1 and Robo2. (F) Optical coronal sections through the IO of wild-type, *Robo1⁻/⁻;Robo2⁻/⁻* or *Robo1⁻/⁻; Robo2^{Δ/Δ}* E13 embryos labeled with Foxp2. In *Robo1⁻/⁻; Robo2⁻/⁻* and *Robo1⁻/⁻;Robo2^{Δ/Δ}* mutants, some Foxp2 IO neurons enter the floor plate (arrowheads). (G) Coronal IO sections of wild type, *Robo1⁻/⁻;Robo2⁻/⁻* or *Robo1⁻/⁻; Robo2^{Δ/Δ}* mutants unilaterally injected with DiI into the cerebellum. In *Robo1⁻/⁻;Robo2⁻/⁻* and *Robo1⁻/⁻;Robo2^{Δ/Δ}* mutants, retrogradely traced IO neurons are found on both the contralateral (contra) and ipsilateral sides (ipsi, arrowhead). (H) IO development in *Ptf1a:Cre;Robo1⁻/⁻; Robo2^{L/L}* mutants. 3D LSFM view (left) of the IO labeled for FoxP2. Note the absence of compaction of the nucleus. The right panels are IO coronal sections of a DiI-injected P0 mouse. DiI-labeled neurons are contralateral to the site of injection. (I) P25 IO coronal sections labeled for Foxp2. The morphology and lamellation of the IO nucleus are similar in *Robo1⁻/⁻;Robo2^{L/L}* and in *Ptf1a:Cre;Robo1⁻/⁻;Robo2^{L/L}* mice. Scale bars: 100 µm.

et al., 2007; Jaworski et al., 2010; Long et al., 2004; López-Bendito et al., 2007; Shu et al., 2003). Spinal cord commissural axons accumulate at the floor plate in *Robo1/Robo2* double knockouts and *Slit1/Slit2/Slit3* triple knockouts (Jaworski et al., 2010; Long et al., 2004), and this is also the case for fasciculus retroflexus axons (Belle et al., 2014). In the cortex, callosal axons fail to cross the midline in Slit and Robo knockouts (Conway et al., 2011; López-Bendito et al., 2007; Shu et al., 2003; Unni et al., 2012).

Apart from one exception (Belle et al., 2014), all these *in vivo* data were obtained in classic Slit and Robo knockouts in which the genes were inactivated in all cells. Slit and Robo knockouts display developmental defects outside the CNS, such as in the kidney (Grieshammer et al., 2004), heart (Mommersteeg et al., 2013, 2015) and vasculature (Rama et al., 2015). Therefore, some of the CNS defects could be related to abnormal function or development of non-neuronal cells that could secondarily alter axon outgrowth and cell migration. Previous work on retinoblastoma (RB) showed that the CNS development was severely perturbed in RB-knockout embryos, including massive apoptosis and precerebellar neuron migration defects (Jacks et al., 1992; Lee et al., 1992). Interestingly, later experiments using chimera and conditional knockouts showed that these anomalies were caused by abnormal placenta development leading to hypoxia (MacPherson et al., 2003; Maandag et al., 1994). This underlines the importance of performing cell-specific inactivation of broadly expressed genes.

Although PN and IO neuron migration is severely perturbed in classic *Robo1/Robo2* knockouts, the selective silencing of Robo1 and Robo2 expression in PN or IO neurons does not lead to significant migration anomalies. PN neurons do not form ectopic chains and IO neurons stop at the midline. This suggests that the defects previously seen in the classic Slit and Robo knockouts are non-cell autonomous. Hoxa2 binds Robo2 genomic sequences and PN migration defects are very similar in *Hoxa2* and *Robo1/Robo2* knockouts (Geisen et al., 2008). However, only a few ectopic PN neurons migrate prematurely in *Wnt1:Cre;Hoxa2^{lox/lox}* mutants (Geisen et al., 2008). These results, together with previous studies in *Drosophila* (Evans et al., 2015; Ordan and Volk, 2015) and mouse (Kaneko et al., 2010) support the existence of non-cell-autonomous function of Slits and Robos in developing neurons. Slits and Robos are expressed in glial cells and neuronal progenitors (Borrell et al., 2012) (and data not shown). In the rostral migratory stream, Slits help sculpting migratory tunnels for neuroblasts (Kaneko et al., 2010) and this could also be the case in the embryonic hindbrain. Interestingly, Ntn1 released at the pial surface by neuronal progenitors rather than floor plate was recently shown to control precerebellar neuron migration (Dominici et al., 2017). These results question the role of floor plate in precerebellar neuron development.

In *Drosophila*, Robo receptors are not expressed at the surface of commissural axons until they have crossed the midline (Kidd et al., 1998). In mouse embryos, our results and previous ones also show
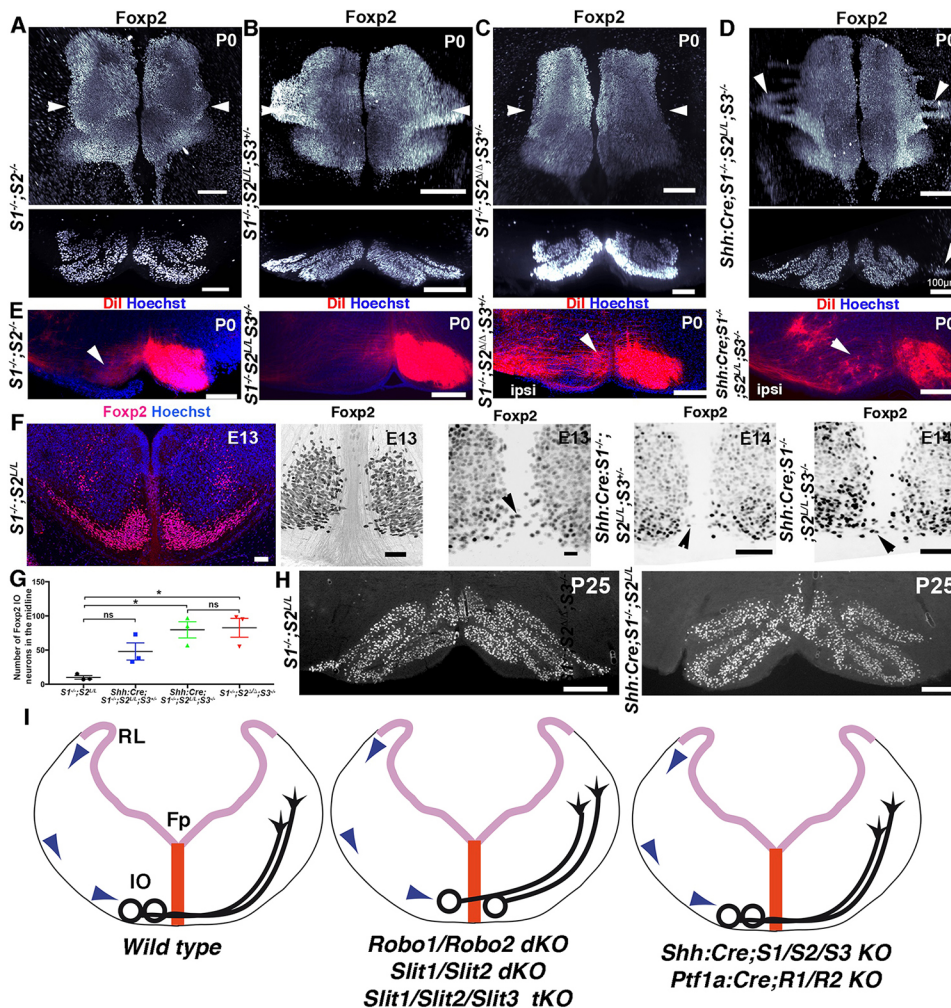
Fig. 9. Slits control the development of the IO nucleus. (A-D) LSFM images of the P0 IO (top panels) and optical sections (lower panels) immunolabeled for Foxp2 and cleared with 3DISCO. In $S1^{-/-};S2^{-/-}$ (A) and, $S1^{-/-};S2^{\Delta/\Delta};S3^{+/-}$ (C) mutants, the IO is abnormal and more compact than wild type (see Fig. 8). IO morphology is normal in $S1^{-/-};S2^{L/L};S3^{+/-}$ (B) mice. (D) In the $Shh:Cre;S1^{-/-};S2^{L/L};S3^{-/-}$ mutant, the morphology of the IO is also perturbed, and neuron-free gaps are seen laterally (arrowheads). (E) Coronal IO section from P0 Slit mutants unilaterally injected with DiI in the cerebellum. In $S1^{-/-};S2^{L/L};S3^{+/-}$ mice, all retrogradely labeled neurons are on the contralateral side, as in wild type. DiI-labeled IO neurons are found in the ipsilateral IO of $S1^{-/-};S2^{-/-}$, $S1^{-/-};S2^{\Delta/\Delta};S3^{+/-}$ and $Shh:Cre;S1^{-/-};S2^{L/L};S3^{-/-}$ mutants (arrowheads). (F) Coronal IO sections of E13 and E14 embryos labeled with Foxp2. In $S1^{-/-};S2^{L/L}$ embryo, IO neurons stop at the midline, whereas in all the other mutants, Foxp2+ IO neurons enter the floor plate (arrowheads). (G) Quantification of the number of Foxp2+ IO neurons invading the midline. *$P<0.05$. ns, not significant ($Shh:Cre;S1^{-/-};S2^{L/L};S3^{+/-}$, $P=0.0891$; Welch's t-test). Error bars indicate s.e.m. (H) Coronal IO sections of P25 mice immunolabeled for Foxp2. IO morphology is perturbed in $Shh:Cre;S1^{-/-};S2^{L/L}$ mutant compared with $S1^{-/-};S2^{L/L}$ mice. The IO is more compact and lamellation is abnormal. (I) Schematic representation of IO defects in Robo and Slit mutants, supporting a non-cell-autonomous action. Scale bars: 200 µm in A, B,E; 100 µm in C,D; 50 µm in F,H.

that Robo1/Robo2 proteins are only detectable in post-crossing axons (Jaworski et al., 2010; Tamada et al., 2008). Therefore, the absence of PN migration defect could be expected if PN neurons do not express Robo1/Robo2 protein during their migration to the midline. Likewise, there is no evidence supporting an expression of Robo1/Robo2 proteins by IO neurons (Di Meglio et al., 2008), and we show here that IO neurons develop normally in *Ptf1a:Cre; Robo1$^{-/-}$;Robo2$^{lox/lox}$* mice. Therefore, the previously described PN and IO migration defects are most likely non-cell-autonomous. Although the selective deletion of Slits in the floor plate, does not seem to have any major effect on precerebellar neurons, it induces significant midline crossing defects at the level of the spinal cord, as reported in *Slit1/Slit2/Slit3* triple knockouts (Long et al., 2004). These results suggest that the sensitivity of commissural neurons to floor-plate-derived guidance cues differs between the hindbrain and the spinal cord.

Interestingly, PN and IO defects in *Slit* conditional knockouts do not phenocopy those found in Robo knockouts. This suggests that Slits might act on precerebellar neurons through other receptors. Slits are cleaved by an unknown protease, into a long N-terminal fragment (Slit-N) and a short C-terminal fragment (Slit-C). Recent studies have show that Slit2-C binds to plexin A1 (Delloye-Bourgeois et al., 2014) and dystroglycan (Wright et al., 2012). In the spinal cord, the floor plate secretes semaphorins and cell-adhesion molecules (CAMs), which are also involved in the control of midline crossing. For example, the gain in responsiveness

of commissural axons to semaphorin 3B repulsion after midline crossing (Nawabi et al., 2010) is stimulated by a soluble form of the neural cell-adhesion molecule (NrCAM). Precerebellar neurons express some components of the receptor complex for semaphorins (Backer et al., 2002; Chen et al., 1997; Gesemann et al., 2001; Vilz et al., 2005) but their function in precerebellar neuron migration is largely unknown and should be studied. For example, NrCAM is expressed by migrating IO neurons (not by PN neurons) but the IO is normal in *Nrcam* knockouts (Backer et al., 2002). Although *in vitro* assays have also confirmed that the floor plate acts as a stop signal for migrating precerebellar neurons (de Diego et al., 2002), our results suggest that repellents other than Slits are involved. It will now be important to extend this strategy to other systems, and re-assess Robo1/Roco2 function in commissural axon guidance in the optic nerve, spinal cord and cortex.

MATERIALS AND METHODS
Mouse strains and genotyping
Slit1/Slit2 (Plump et al., 2002), *Slit3* (Yuan et al., 2003), *Robo1* (Long et al., 2004), *Robo2* (Grieshammer et al., 2004), *Robo3lox* (Renier et al., 2010), *Robo2lox* (Gibson et al., 2014) and *Slit2lox* (Rama et al., 2015) knockouts, and *Shh:Cre* (Harfe et al., 2004), *Wnt1:Cre* (Danielian et al., 1998), *Krox20: Cre* (Voiculescu et al., 2000), *Ptf1a:Cre* (Kawaguchi et al., 2002), *Phox2b: Cre* (Pattyn et al., 2000) and *Tau^{GFP}* (Hippenmeyer et al., 2005) lines were previously described and genotyped by PCR. Wild-type mice were from the C57BL6 background (Janvier, France). Compound mutants were obtained by intercrosses. The day of the vaginal plug was counted as E0.5 and the day

of the birth as postnatal day 0 (P0). From E16 to P0, the nervous system was dissected and fixed at 4°C overnight by immersion in 4% paraformaldehyde (PFA; Merck) in 0.1 M phosphate buffer (pH 7.4). P15-P25 mice were anesthetized with ketamine (100 mg/ml) and xylazine (10 mg/ml), and perfused using 4% PFA. All animal procedures were carried out in accordance to institutional guidelines (UPMC Comité Charles Darwin). Mice of either sex were used and no animals were excluded. All data quantification was carried out by an observer blinded to the experimental conditions. We did not perform randomization into groups.

Immunohistochemistry on brain sections
Embryos and adult brains were cryoprotected in 10% sucrose (in 0.1 M phosphate buffer) for cryostat sectioning. Cryostat sections (20 µm) were blocked in PBS containing 0.2% gelatin and 0.25% Triton X-100, and incubated overnight at room temperature with primary antibodies against goat anti-Robo3 (1:300, R&D System, AF3076), rabbit anti-Barhl1 (1:500, Sigma, HPA004809), goat anti-ChAT (1:100, Millipore, AB144P), goat anti-Dcc (1:500, Santa Cruz, sc-6535), rabbit anti-Foxp2 (1:1000, Abcam, ab16046), chicken anti-GFP (1:800, Abcam, ab13970), goat anti-Robo1 (1:500, R&D System, AF1749), rabbit anti-Robo2 (against peptide QNQSQRPRPTKKHKGGRMDP; 1:800, Biotem), goat anti-Tag-1 (1:1000, R&D Systems, AF4439) and rabbit anti-islet1 (1:500, Abcam, ab20670). The following secondary antibodies were used: bovine anti-goat and donkey anti-rabbit, coupled to CY3 or CY5 (1:600, Jackson Laboratories; 805-165-180, 805-605-180, 711-165-152 and 711-175-152), donkey anti-chicken coupled to Alexa Fluor 488 (1:600, Invitrogen, A-11039) and donkey anti-rabbit coupled to Alexa Fluor 647 (1:600, Jackson Laboratories, 711-605-152). Sections counterstained with Hoechst 33258 (10 mg/ml, Sigma, B2883) were imaged with a fluorescent microscope (DM6000, Leica) coupled to a CoolSnapHQ camera (Roper Scientific), a Nanozoomer (Hamamatsu) or an upright confocal microscope (Olympus FV1000).

In utero electroporation
In utero electroporation of pCX-EGFP (1 µg/µl) plasmid (provided by Dr M. Okabe, Osaka University, Japan) PN neurons was performed as described previously (Zelina et al., 2014).

DiI tracing
The 4% PFA-fixed P0 animals were injected into the cerebellum with small crystals of 1,1′-dioctadecyl-3,3,3′,3′-tetramethylindocarbocyanine (DiI; Invitrogen) using glass micropipettes. Injected brains were kept at 37°C for 3 weeks. Brains were cut at 100 µm with a vibratome (Leica), counterstained with Hoechst and imaged by an upright confocal microscope (Olympus FV1000).

In situ hybridization
Antisense riboprobes were labeled with DIG (digoxigenin-11-UTP, Roche) as described previously (Marillat et al., 2002) by *in vitro* transcription of mouse cDNA encoding *Slit1* (Nguyen-Ba-Charvet et al., 2004), *Slit2* exon 8 (Rama et al., 2015), *Slit3* (Rama et al., 2015), *Ntn1* (Serafini et al., 1996) and *Robo2* exon 5 (Gibson et al., 2014). *In situ* hybridization was performed as described previously (Marillat et al., 2002) and tissue sections were imaged using a Nanozoomer slide scanner (Hamamatsu).

Whole-mount immunostaining and tissue clearing
The procedure was similar for single and multiple labeling and has been described previously (Belle et al., 2014). Clearing was performed according to the 3DISCO procedure (Ertürk et al., 2011), with slight modifications (Belle et al., 2014).

3D imaging and image processing
3D imaging was primarily performed with an ultramicroscope (LaVision BioTec) using InspectorPro software (LaVision BioTec) or with an upright confocal microscope (Olympus FV1000). 3D volume images were generated using Imaris ×64 software (version 7.6.1, Bitplane). Stack images were first converted to imaris file (.ims) using Imaris FileConverter.

File size was next reduced to 8 bits. 3D reconstruction of the samples was performed using 'volume rendering' (Imaris). The sample could be optically sliced in any angle using the 'orthoslicer' or 'obliqueslicer' tools. Air bubbles and crystals that might form at the surface of the samples could be eliminated using the 'surface' tool by creating a mask around each volume. 3D pictures and movies were generated using the 'snapshot' and 'animation' tools. Finally, images were cropped and, if required, their brightness was adjusted evenly using Photoshop CS4 (Adobe).

Statistical analysis
To quantify the number of Foxp2$^+$ IO neurons invading the midline, eight series of 20 µm cryosections were obtained from E13 and E14 hindbrains. On each section, a 40 µm region at the midline was chosen and the number of Foxp2$^+$ IO neurons was counted using ImageJ Software (n=3 embryos for each genotype). For statistical analyses, an unpaired t-test was used. To quantify PN migration defects, the total distance separating the caudal-most and rostral-most Barhl1$^+$/Robo3 neurons along the midline was measured using the measurement tool (Imaris, Bitplane Software; n=3-5 cases for each genotype). For statistical analysis, a Welch's t-test was used. Compiled data are expressed as mean±s.e.m. Statistical analyses were performed with Prism 7 (GraphPad Software).

Competing interests
The authors declare no competing or financial interests.

Author contributions
Conceptualization: A.C.; Methodology: C.D., Q.R., P.Z., S.F., A.C.; Validation: S.F., A.C.; Formal analysis: C.D., Q.R., P.Z., A.C.; Investigation: C.D., Q.R., P.Z., S.F., A.C.; Resources: A.C.; Data curation: C.D., Q.R., P.Z., S.F., A.C.; Writing - original draft: A.C.; Writing - review & editing: C.D., P.Z., A.C.; Visualization: A.C.; Supervision: A.C.; Project administration: A.C.; Funding acquisition: A.C.

Supplementary information
Supplementary information available online at
http://dev.biologists.org/lookup/doi/10.1242/dev.150375.supplemental

References
Altman, J. and Bayer, S. A. (1987). Development of the precerebellar nuclei in the rat: I. The precerebellar neuroepithelium of the rhombencephalon. *J. Comp. Neurol.* **257**, 477-489.

Azizi, S. A. and Woodward, D. J. (1987). Inferior olivary nuclear complex of the rat: morphology and comments on the principles of organization within the olivocerebellar system. *J. Comp. Neurol.* **263**, 467-484.

Backer, S., Sakurai, T., Grumet, M., Sotelo, C. and Bloch-Gallego, E. (2002). Nr-CAM an TAG-1 are expressed in distinct populations of developing precerebellar and cerebellar neurons. *Neuroscience* **113**, 743-748.

Badura, A., Schoneville, M., Voges, K., Galliano, E., Renier, N., Gao, Z., Witter, L., Hoebeek, F. E., Chédotal, A. and De Zeeuw, C. I. (2013). Climbing fiber input shapes reciprocity of purkinje cell firing. *Neuron* **78**, 700-713.

Bagri, A., Marin, O., Plump, A. S., Mak, J., Pleasure, S. J., Rubenstein, J. L. R. and Tessier-Lavigne, M. (2002). Slit proteins prevent midline crossing and determine the dorsoventral position of major axonal pathways in the mammalian forebrain. *Neuron* **33**, 233-248.

Belle, M., Godefroy, D., Dominici, C., Heitz-Marchaland, C., Zelina, P., Hellal, F., Bradke, F. and Chédotal, A. (2014). A simple method for 3D analysis of immunolabeled axonal tracts in a transparent nervous system. *Cell Rep.* **9**, 1191-1201.

Bloch-Gallego, E., Ezan, F., Tessier-Lavigne, M. and Sotelo, C. (1999). Floor plate and netrin-1 are involved in the migration and survival of inferior olivary neurons. *J. Neurosci.* **19**, 4407-4420.

Blockus, H. and Chédotal, A. (2016). Slit-Robo signaling. *Development* **143**, 3037-3044.

Borrell, V., Cárdenas, A., Ciceri, G., Galcerán, J., Flames, N., Pla, R., Nóbrega-Pereira, S., García-Frigola, C., Peregrín, S., Zhao, Z. et al. (2012). Slit/Robo signaling modulates the proliferation of central nervous system progenitors. *Neuron* 76, 338-352.

Bourrat, F. and Sotelo, C. (1988). Migratory pathways and neuritic differentiation of inferior olivary neurons in the rat embryo. Axonal tracing study using the in vitro slab technique. *Brain Res.* 467, 19-37.

Brose, K., Bland, K. S., Wang, K. H., Arnott, D., Henzel, W., Goodman, C. S., Tessier-Lavigne, M. and Kidd, T. (1999). Slit proteins bind Robo receptors and have an evolutionarily conserved role in repulsive axon guidance. *Cell* 96, 795-806.

Chédotal, A. (2011). Further tales of the midline. *Curr. Opin. Neurobiol.* 21, 68-75.

Chen, H., Chédotal, A., He, Z., Goodman, C. S. and Tessier-Lavigne, M. (1997). Neuropilin-2, a novel member of the neuropilin family, is a high affinity receptor for the semaphorins Sema E and Sema IV but not Sema III. *Neuron* 19, 547-559.

Conway, C. D., Howe, K. M., Nettleton, N. K., Price, D. J., Mason, J. O. and Pratt, T. (2011). Heparan sulfate sugar modifications mediate the functions of slits and other factors needed for mouse forebrain commissure development. *J. Neurosci.* 31, 1955-1970.

Danielian, P. S., Muccino, D., Rowitch, D. H., Michael, S. K. and McMahon, A. P. (1998). Modification of gene activity in mouse embryos in utero by a tamoxifen-inducible form of Cre recombinase. *Curr. Biol.* 8, 1323-1326.

de Diego, I., Kyriakopoulou, K., Karagogeos, D. and Wassef, M. (2002). Multiple influences on the migration of precerebellar neurons in the caudal medulla. *Development* 129, 297-306.

Delloye-Bourgeois, C., Jacquier, A., Charoy, C., Reynaud, F., Nawabi, H., Thoinet, K., Kindbeiter, K., Yoshida, Y., Zagar, Y., Kong, Y. et al. (2014). PlexinA1 is a new Slit receptor and mediates axon guidance function of Slit C-terminal fragments. *Nat. Neurosci.* 18, 36-45.

Di Meglio, T., Nguyen-Ba-Charvet, K. T., Tessier-Lavigne, M., Sotelo, C. and Chédotal, A. (2008). Molecular mechanisms controlling midline crossing by precerebellar neurons. *J. Neurosci.* 28, 6285-6294.

Di Meglio, T., Vitobello, A., Yonehara, K., Hrycaj, S. M., Roska, B., Kratochwil, C. F., Vilain, N., Loche, A., Peters, A. H. F. M., Eichmann, A. et al. (2013). Ezh2 orchestrates topographic migration and connectivity of mouse precerebellar neurons. *Science* 339, 204-207.

Dominici, C., Moreno-Bravo, J. A., Roig Puiggros, S., Rappeneau, Q., Rama, N., Vieugue, P., Bernet, A., Mehlen, P. and Chédotal, A. (2017). Floor-plate-derived netrin-1 is dispensable for commissural axon guidance. *Nature* 545, 350-354.

Ertürk, A., Mauch, C. P., Hellal, F., Förstner, F., Keck, T., Becker, K., Jährling, N., Steffens, H., Richter, M., Hübener, M. et al. (2011). Three-dimensional imaging of the unsectioned adult spinal cord to assess axon regeneration and glial responses after injury. *Nat. Med.* 18, 166-171.

Essick, C. R. (1907). The corpus ponto-bulbare, a hitherto undescribed nuclear mass in the human hind brain. *Am. J. Anat.* 7, 119-135.

Essick, C. R. (1912). The development of the nuclei pontis and the nucleus arcuatus in man. *Am. J. Anat.* 13, 25-54.

Evans, T. A., Santiago, C., Arbeille, E. and Bashaw, G. J. (2015). Robo2 acts in trans to inhibit Slit-Robo1 repulsion in pre-crossing commissural axons. *Elife* 4, 1-26.

Fouquet, C., Di Meglio, T., Ma, L., Kawasaki, T., Long, H., Hirata, T., Tessier-Lavigne, M., Chédotal, A. and Nguyen-Ba-Charvet, K. T. (2007). Robo1 and robo2 control the development of the lateral olfactory tract. *J. Neurosci.* 27, 3037-3045.

Fricke, C., Lee, J.-S., Geiger-Rudolph, S., Bonhoeffer, F. and Chien, C.-B. (2001). astray, a zebrafish roundabout homolog required for retinal axon guidance. *Science* 292, 507-510.

Fujita, H. and Sugihara, I. (2012). FoxP2 expression in the cerebellum and inferior olive: development of the transverse stripe-shaped expression pattern in the mouse cerebellar cortex. *J. Comp. Neurol.* 520, 656-677.

Geisen, M. J., Di Meglio, T., Pasqualetti, M., Ducret, S., Brunet, J.-F., Chédotal, A., Rijli, F. M. and Zoghbi, H. Y. (2008). Hox paralog group 2 genes control the migration of mouse pontine neurons through slit-robo signaling. *PLoS Biol.* 6, e142.

Gesemann, M., Litwack, E. D., Yee, K. T., Christen, U. and O'Leary, D. D. M. (2001). Identification of candidate genes for controlling development of the basilar pons by differential display PCR. *Mol. Cell. Neurosci.* 18, 1-12.

Gibson, D. A., Tymanskyj, S., Yuan, R. C., Leung, H. C., Lefebvre, J. L., Sanes, J. R., Chédotal, A. and Ma, L. (2014). Dendrite self-avoidance requires cell-autonomous slit/robo signaling in cerebellar purkinje cells. *Neuron* 81, 1040-1056.

Grieshammer, U., Ma, L., Plump, A. S., Wang, F., Tessier-lavigne, M. and Martin, G. R. (2004). SLIT2-mediated ROBO2 signaling restrict kidney induction to a single site. *Dev. Cell* 6, 709-717.

Harfe, B. D., Scherz, P. J., Nissim, S., Tian, H., McMahon, A. P. and Tabin, C. J. (2004). Evidence for an expansion-based temporal Shh gradient in specifying vertebrate digit identities. *Cell* 118, 517-528.

Harkmark, W. (1954). Cell migrations from the rhombic lip to the inferior olive, the nucleus raphe and the pons. A morphological and experimental investigation of the chick embryo. *J. Comp. Neurol.* 100, 115-209.

Hippenmeyer, S., Vrieseling, E., Sigrist, M., Portmann, T., Laengle, C., Ladle, D. R. and Arber, S. (2005). A developmental switch in the response of DRG neurons to ETS transcription factor signaling. *PLoS Biol.* 3, e159.

His, W. (1891). Die Entwickelung des menschlichen Rautenhirns vom Ende des ersten bis zum Beginn des dritten Monats. *Abhandlungen der königlich sächsischen Gesellschaft der Wissenschaften, Math. Klasse* 29, 1-74.

Jacks, T., Fazeli, A., Schmitt, E. M., Bronson, R. T., Goodell, M. A. and Weinberg, R. A. (1992). Effects of an Rb mutation in the mouse. *Nature* 359, 295-300.

Jaworski, A., Long, H. and Tessier-Lavigne, M. (2010). Collaborative and specialized functions of Robo1 and Robo2 in spinal commissural axon guidance. *J. Neurosci.* 30, 9445-9453.

Jen, J. C., Chan, W.-M. M., Bosley, T. M., Wan, J., Carr, J. R., Rub, U., Shattuck, D., Salamon, G., Kudo, L. C., Ou, J. et al. (2004). Mutations in a human ROBO gene disrupt hindbrain axon pathway crossing and morphogenesis. *Science* 304, 1509-1513.

Joksimovic, M., Yun, B. A., Kittappa, R., Anderegg, A. M., Chang, W. W., Taketo, M. M., McKay, R. D. G. and Awatramani, R. B. (2009). Wnt antagonism of Shh facilitates midbrain floor plate neurogenesis. *Nat. Neurosci.* 12, 125-131.

Kaneko, N., Marín, O., Koike, M., Hirota, Y., Uchiyama, Y., Wu, J. Y., Lu, Q., Tessier-Lavigne, M., Alvarez-Buylla, A., Okano, H. et al. (2010). New neurons clear the path of astrocytic processes for their rapid migration in the adult brain. *Neuron* 67, 213-223.

Kawaguchi, Y., Cooper, B., Gannon, M., Ray, M., MacDonald, R. J. and Wright, C. V. E. (2002). The role of the transcriptional regulator Ptf1a in converting intestinal to pancreatic progenitors. *Nat. Genet.* 32, 128-134.

Kawauchi, D., Taniguchi, H., Watanabe, H., Saito, T. and Murakami, F. (2006). Direct visualization of nucleogenesis by precerebellar neurons: involvement of ventricle-directed, radial fibre-associated migration. *Development* 133, 1113-1123.

Kidd, T., Brose, K., Mitchell, K. J., Fetter, R. D., Tessier-Lavigne, M., Goodman, C. S. and Tear, G. (1998). Roundabout controls axon crossing of the CNS midline and defines a novel subfamily of evolutionarily conserved guidance receptors. *Cell* 92, 205-215.

Kidd, T., Bland, K. S. and Goodman, C. S. (1999). Slit is the midline repellent for the robo receptor in Drosophila. *Cell* 96, 785-794.

Lee, E. Y.-H. P., Chang, C.-Y., Hu, N., Wang, Y.-C. J., Lai, C.-C., Herrup, K., Lee, W.-H. and Bradley, A. (1992). Mice deficient for Rb are nonviable and show defects in neurogenesis and haematopoiesis. *Nature* 359, 288-294.

Long, H., Sabatier, C., Ma, L., Plump, A. S., Yuan, W., Ornitz, D. M., Tamada, A., Murakami, F., Goodman, C. S. and Tessier-Lavigne, M. (2004). Conserved roles for Slit and Robo proteins in midline commissural axon guidance. *Neuron* 42, 213-223.

López-Bendito, G., Flames, N., Ma, L., Fouquet, C., Di Meglio, T., Chédotal, A., Tessier-Lavigne, M. and Marin, O. (2007). Robo1 and Robo2 cooperate to control the guidance of major axonal tracts in the mammalian forebrain. *J. Neurosci.* 27, 3395-3407.

Maandag, E. C., van der Valk, M., Vlaar, M., Feltkamp, C., O'Brien, J., van Roon, M., van der Lugt, N., Berns, A. and te Riele, H. (1994). Developmental rescue of an embryonic-lethal mutation in the retinoblastoma gene in chimeric mice. *EMBO J.* 13, 4260-4268.

MacPherson, D., Sage, J., Crowley, D., Trumpp, A., Bronson, R. T. and Jacks, T. (2003). Conditional mutation of Rb causes cell cycle defects without apoptosis in the central nervous system. *Mol. Cell. Biol.* 23, 1044-1053.

Marcos, S., Backer, S., Causeret, F., Tessier-Lavigne, M. and Bloch-Gallego, E. (2009). Differential roles of Netrin-1 and its receptor DCC in inferior olivary neuron migration. *Mol. Cell. Neurosci.* 41, 429-439.

Marillat, V., Chédotal, A., Cases, O., Nguyen-Ba-Charvet, K. T., Tessier-Lavigne, M. and Sotelo, C. (2002). Spatiotemporal expression patterns of slit and robo genes in the rat brain. *J. Comp. Neurol.* 442, 130-155.

Marillat, V., Sabatier, C., Failli, V., Matsunaga, E., Sotelo, C., Tessier-Lavigne, M. and Chédotal, A. (2004). The slit receptor Rig-1/Robo3 controls midline crossing by hindbrain precerebellar neurons and axons. *Neuron* 43, 69-79.

Mommersteeg, M. T. M., Andrews, W. D., Ypsilanti, A. R., Zelina, P., Yeh, M. L., Norden, J., Kispert, A., Chédotal, A., Christoffels, V. M. and Parnavelas, J. G. (2013). Slit-roundabout signaling regulates the development of the cardiac systemic venous return and pericardium. *Circ. Res.* 112, 465-475.

Mommersteeg, M. T. M., Yeh, M. L., Parnavelas, J. G. and Andrews, W. D. (2015). Disrupted Slit-Robo signalling results in membranous ventricular septum defects and bicuspid aortic valves. *Cardiovasc. Res.* 106, 55-66.

Nawabi, H., Briançon-Marjollet, A., Clark, C., Sanyas, I., Takamatsu, H., Okuno, T., Kumanogoh, A., Bozon, M., Takeshima, K., Yoshida, Y. et al. (2010). A midline switch of receptor processing regulates commissural axon guidance in vertebrates. *Genes Dev.* 24, 396-410.

Nguyen-Ba-Charvet, K. T., Plump, A. S., Tessier-Lavigne, M. and Chédotal, A. (2002). Slit1 and slit2 proteins control the development of the lateral olfactory tract. *J. Neurosci.* 22, 5473-5480.

Nguyen-Ba-Charvet, K. T., Picard-Riera, N., Tessier-Lavigne, M., Baron-Van Evercooren, A., Sotelo, C. and Chédotal, A. (2004). Multiple roles for slits in the control of cell migration in the rostral migratory stream. *J. Neurosci.* 24, 1497-1506.

Nichols, D. H. and Bruce, L. L. (2006). Migratory routes and fates of cells transcribing the Wnt-1 gene in the murine hindbrain. *Dev. Dyn.* **235**, 285-300.

Ordan, E. and Volk, T. (2015). A non-signaling role of Robo2 in tendons is essential for Slit processing and muscle patterning. *Development* **142**, 3512-3518.

Pattyn, A., Hirsch, M., Goridis, C. and Brunet, J. F. (2000). Control of hindbrain motor neuron differentiation by the homeobox gene Phox2b. *Development* **127**, 1349-1358.

Plachez, C., Andrews, W., Liapi, A., Knoell, B., Drescher, U., Mankoo, B., Zhe, L., Mambetisaeva, E., Annan, A., Bannister, L. et al. (2008). Robos are required for the correct targeting of retinal ganglion cell axons in the visual pathway of the brain. *Mol. Cell. Neurosci.* **37**, 719-730.

Plump, A. S., Erskine, L., Sabatier, C., Brose, K., Epstein, C. J., Goodman, C. S., Mason, C. A. and Tessier-Lavigne, M. (2002). Slit1 and Slit2 cooperate to prevent premature midline crossing of retinal axons in the mouse visual system. *Neuron* **33**, 219-232.

Rama, N., Dubrac, A., Mathivet, T., Ní Chárthaigh, R.-A., Genet, G., Cristofaro, B., Pibouin-Fragner, L., Ma, L., Eichmann, A. and Chédotal, A. (2015). Slit2 signaling through Robo1 and Robo2 is required for retinal neovascularization. *Nat. Med.* **21**, 483-491.

Renier, N., Schonewille, M., Giraudet, F., Badura, A., Tessier-Lavigne, M., Avan, P., De Zeeuw, C. I. and Chédotal, A. (2010). Genetic dissection of the function of hindbrain axonal commissures. *PLoS Biol.* **8**, e1000325.

Rodriguez, C. I. and Dymecki, S. M. (2000). Origin of the precerebellar system. *Neuron* **27**, 475-486.

Sabatier, C., Plump, A. S., Ma, L., Brose, K., Tamada, A., Murakami, F., Lee, E. Y.-H. P. and Tessier-Lavigne, M. (2004). The divergent Robo family protein rig-1/Robo3 is a negative regulator of slit responsiveness required for midline crossing by commissural axons. *Cell* **117**, 157-169.

Seeger, M., Tear, G., Ferres-Marco, D. and Goodman, C. S. (1993). Mutations affecting growth cone guidance in Drosophila: genes necessary for guidance toward or away from the midline. *Neuron* **10**, 409-426.

Serafini, T., Colamarino, S. A., Leonardo, E. D., Wang, H., Beddington, R., Skarnes, W. C. and Tessier-Lavigne, M. (1996). Netrin-1 is required for commissural axon guidance in the developing vertebrate nervous system. *Cell* **87**, 1001-1014.

Shu, T., Sundaresan, V., McCarthy, M. M. and Richards, L. J. (2003). Slit2 guides both precrossing and postcrossing callosal axons at the midline in vivo. *J. Neurosci.* **23**, 8176-8184.

Sotelo, C. and Chédotal, A. (2013). Hindbrain tangential migration. In *Comprehensive Developmental Neuroscience: Cellular Migration and Formation of Neuronal Connections* (ed. J. L. R. Rubenstein and P. Rakic), pp. 345-362. Amsterdam, The Nethlands: Elsevier

Tamada, A., Kumada, T., Zhu, Y., Matsumoto, T., Hatanaka, Y., Muguruma, K., Chen, Z., Tanabe, Y., Torigoe, M., Yamauchi, K. et al. (2008). Crucial roles of Robo proteins in midline crossing of cerebellofugal axons and lack of their up-regulation after midline crossing. *Neural Dev.* **3**, 29.

Unni, D. K., Piper, M., Moldrich, R. X., Gobius, I., Liu, S., Fothergill, T., Donahoo, A.-L. S., Baisden, J. M., Cooper, H. M. and Richards, L. J. (2012). Multiple Slits regulate the development of midline glial populations and the corpus callosum. *Dev. Biol.* **365**, 36-49.

Vilz, T. O., Moepps, B., Engele, J., Molly, S., Littman, D. R. and Schilling, K. (2005). The SDF-1/CXCR4 pathway and the development of the cerebellar system. *Eur. J. Neurosci.* **22**, 1831-1839.

Voiculescu, O., Charnay, P. and Schneider-Maunoury, S. (2000). Expression pattern of a Krox-20/Cre knock-in allele in the developing hindbrain, bones, and peripheral nervous system. *Genesis* **26**, 123-126.

Watanabe, H. and Murakami, F. (2009). Real time analysis of pontine neurons during initial stages of nucleogenesis. *Neurosci. Res.* **64**, 20-29.

Weiner, J. A., Koo, S. J., Nicolas, S., Fraboulet, S., Pfaff, S. L., Pourquié, O. and Sanes, J. R. (2004). Axon fasciculation defects and retinal dysplasias in mice lacking the immunoglobulin superfamily adhesion molecule BEN/ALCAM/SC1. *Mol. Cell. Neurosci.* **27**, 59-69.

Wolfer, D. P., Henehan-Beatty, A., Stoeckli, E. T., Sonderegger, P. and Lipp, H.-P. (1994). Distribution of TAG-1/axonin-1 in fibre tracts and migratory streams of the developing mouse nervous system. *J. Comp. Neurol.* **345**, 1-32.

Wright, K. M., Lyon, K. A., Leung, H., Leahy, D. J., Ma, L. and Ginty, D. D. (2012). Dystroglycan organizes axon guidance cue localization and axonal pathfinding. *Neuron* **76**, 931-944.

Yee, K. T., Simon, H. H., Tessier-Lavigne, M. and O'Leary, D. D. M. (1999). Extension of long leading processes and neuronal migration in the mammalian brain directed by the chemoattractant netrin-1. *Neuron* **24**, 607-622.

Ypsilanti, A. R., Zagar, Y. and Chédotal, A. (2010). Moving away from the midline: new developments for Slit and Robo. *Development* **137**, 1939-1952.

Yuan, W., Rao, Y., Babiuk, R. P., Greer, J. J., Wu, J. Y. and Ornitz, D. M. (2003). A genetic model for a central (septum transversum) congenital diaphragmatic hernia in mice lacking Slit3. *Proc. Natl. Acad. Sci. USA* **100**, 5217-5222.

Zallen, J. A., Kirch, S. A. and Bargmann, C. I. (1999). Genes required for axon pathfinding and extension in the C. *elegans nerve ring*. *Development* **126**, 3679-3692.

Zelina, P., Blockus, H., Zagar, Y., Péres, A., Friocourt, F., Wu, Z., Rama, N., Fouquet, C., Hohenester, E., Tessier-Lavigne, M. et al. (2014). Signaling switch of the axon guidance receptor Robo3 during vertebrate evolution. *Neuron* **84**, 1-15.

Supplementary Materials

Non-cell autonomous control of precerebellar neuron migration by Slits and Robos.

Chloé Dominici, Quentin Rappeneau, Pavol Zelina, Stéphane Fouquet and Alain Chédotal.
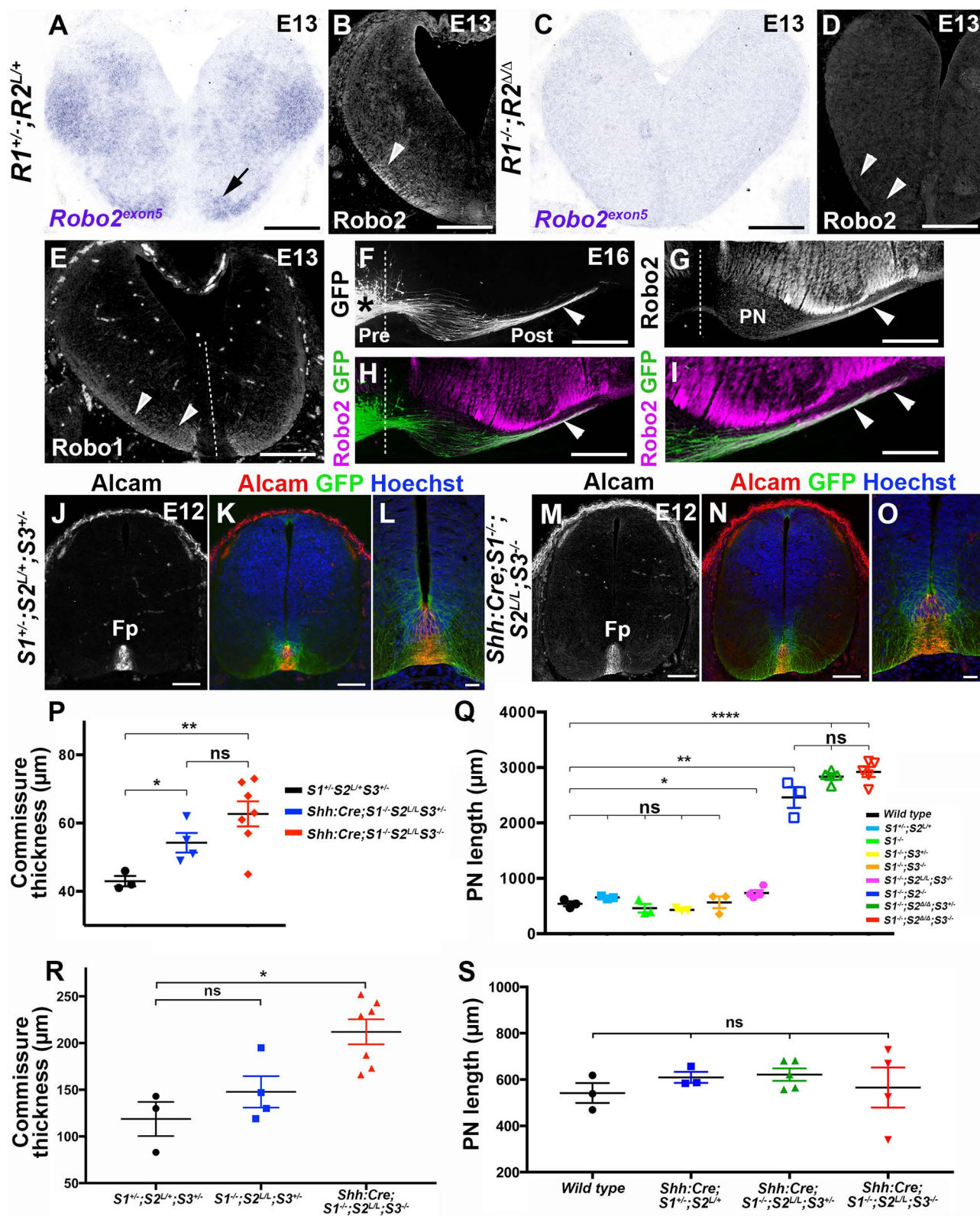
Figure S1

Figure S1

Validation of precerebellar neuron defects in Slit and Robo mutants.

(A-D) Sections of E13 hindbrains, at the level of the inferior olive (arrow in A), hybridized with a *Robo2* exon5 specific probe (A, C) or immunolabeled with an anti-Robo2 antibody (B, D). Robo2 mRNA is not detected in *Robo1$^{-/-}$;Robo2$^{\Delta/\Delta}$* embryo compared to *Robo1$^{+/-}$;Robo2$^{L/+}$* embryo. Likewise, Robo2-immunoreactive processes seen in *Robo1$^{+/-}$;Robo2$^{L/+}$* embryos are absent in *Robo1$^{-/-}$;Robo2$^{\Delta/\Delta}$* mutant (arrowheads). (E) E13 hindbrain sections immunolabeled for Robo1. Robo1 is detected laterally in longitudinal axons (arrowheads) but not at the level of the floor plate (dashed lines). (F-I) Coronal sections at the level of the pontine nuclei (PN) of an E16 wild type embryo unilaterally electroporated at E13.5 with pCX-GFP and immunolabeled with Robo2 antibodies. GFP+ PN neurons (arrowhead in F) accumulate at the midline (dashed line) but their axons cross it and extend on the opposite side (arrowheads). Robo2 is highly expressed in hindbrain axons but not detected in PN neuron cell bodies. However, Robo2 is present on post-crossing PN axons (arrowhead in G-I). (J-O) Spinal cord sections of E12 *S1$^{+/-}$;S2$^{+/-}$;S3$^{+/-}$* (J-L) and *Shh:Cre;S1$^{-/-}$;S2$^{L/L}$;S3$^{-/-}$* (M-O) embryos immunolabeled with antibodies against Alcam and GFP. The floor plate (Fp) is labeled and similar in controls and mutants. (P) Quantification of spinal cord commissure thickness in *Shh:Cre;Slit* mutants (relates to Fig. 4). ns, not significant, P=0.1035. (Q) Quantification of PN nuclei length in *Slit* double and triple mutants (relates to Figs. 5-7). Comparison between wild type and each genotype. ns: *S1$^{+/-}$;S2$^{L/+}$*, P=0.1080 ; *S1$^{-/-}$*, P=0.4221 ; *S1$^{-/-}$;S3$^{+/-}$*, P=0.1130; *S1$^{-/-}$;S3$^{-/-}$*; P=0.8440). (R) Quantification of hindbrain commissure thickness in E12 *Slit* mutants (relates to Fig. 6). ns, *S1$^{-/-}$;S2$^{L/L}$;S3$^{+/-}$*, P=0.2973. (S) Quantification of PN nuclei length in *Shh:Cre;Slit* mutants (relates to Fig. 6). Comparison between wild type and other genotypes. ns, *Shh:Cre;S1$^{+/-}$;S2$^{L/+}$*, P=0.2613 ; *Shh:Cre;S1$^{-/-}$;S2$^{L/L}$;S3$^{+/-}$*,P=0.2008; *Shh:Cre;S1$^{-/-}$;S2$^{L/L}$;S3$^{-/-}$* , P=0.8173. *P<0.05, **P<0.01, ***P<0.001 and ****P<0.0001. Welch's t-test. Error bar indicate standard error of the mean (s.e.m.).

Abbreviations: Pre, pre-crossing; Post, post-crossing.

Scale bars: 275 μm (A), 250 μm (B, C), 200 μm (D, E), 150 μm (F-G), 50 μm (I), 80 μm (J,K,M,N), 20 μm (L, O).
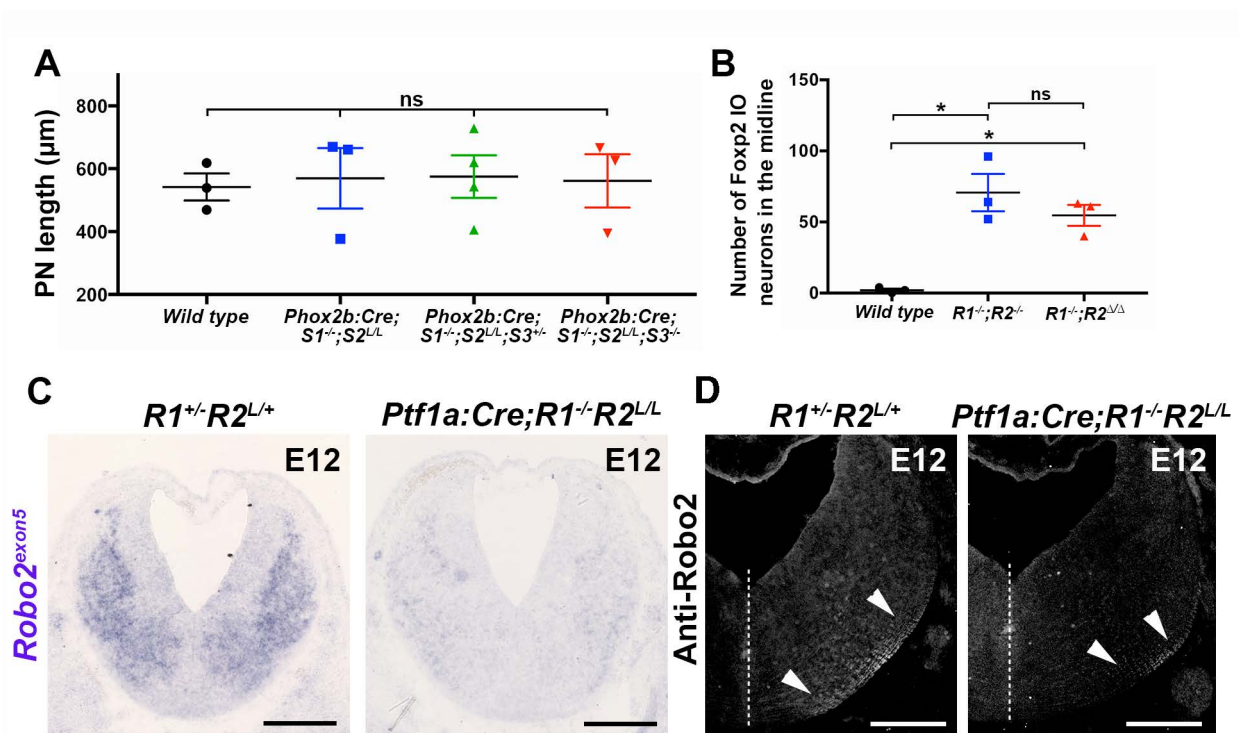
Figure S2

Validation of Robo2 inactivation in *Ptf1a:Cre;Robo1/2* mutants.

(A) Quantification of pontine neuron (PN) length in Phox2b:Cre;Slit1/2/3 mutants. (B) Quantification of the number of Foxp2+ IO neurons invading the midline in Robo1/2 double mutants. Comparison between wild type and other genotypes. *P<0,05. ns, *Phox2b:Cre;S1$^{-/-}$;S2$^{L/L}$*, P=0.8134; *Phox2b:Cre;S1$^{-/-}$;S2$^{L/L}$;S3$^{+/-}$*, P=0.6994 ; *Phox2b:Cre;S1$^{-/-}$;S2$^{L/L}$;S3$^{-/-}$*, P=0.8493 (Welch's t-test). Error bar indicate standard error of the mean (s.e.m.). (C, D) Sections of E12 hindbrains, at the level of the inferior olive, hybridized with a *Robo2* exon5 specific probe (C) or immunolabeled with an anti-Robo2 antibody (D). Robo2 mRNA expression is strongly downregulated in *Ptf1a:Cre;Robo1$^{-/-}$;Robo2$^{L/L}$* embryos (left panels) compared to *Robo1$^{+/-}$;Robo2$^{L/+}$* embryos (right panels). Likewise, the density of Robo2+ immunoreactive axons is also decreased (arrowheads). Dashed lines indicate the midline. Scale bars: 300µm (C), 250µm (D).

Movies

Movie 1

3D movie of the migrating stream of pontine neurons in a wild type E16 embryo.

Whole-mount immunolabeling for Barhl1 (Green) and Robo3 (Red) and 3DISCO clearing.

Movie 2

3D movie of the migrating stream of pontine neurons in a *Robo1$^{-/-}$;Robo2$^{-/-}$* E16 embryo.

Whole-mount immunolabeling for Barhl1 (Green) and Robo3 (Red) and 3DISCO clearing.

Movie 3

3D movie of the migrating stream of pontine neurons in a *Robo1$^{-/-}$;Robo2$^{Δ/Δ}$* E16 embryo.

Whole-mount immunolabeling for Barhl1 (Green) and Robo3 (Red) and 3DISCO clearing.

Movie 4

3D movie of the migrating stream of pontine neurons in a *Slit1$^{-/-}$;Slit2$^{-/-}$* E16 embryo.

Whole-mount immunolabeling for Barhl1 (Green) and Robo3 (Red) and 3DISCO clearing.

Movie 5

3D movie of the migrating stream of pontine neurons in a *Slit1^{-/-};Slit2^{-/-};Slit3^{-/-}* E16 embryo.

Whole-mount immunolabeling for Barhl1 (Green) and Robo3 (Red) and 3DISCO clearing.

Movie 6

3D movie of the migrating stream of pontine neurons in a *Slit1^{-/-};Slit2^{Δ/Δ};Slit3^{-/-}* E16 embryo. Whole-mount immunolabeling for Barhl1 (Green) and Robo3 (Red) and 3DISCO clearing.
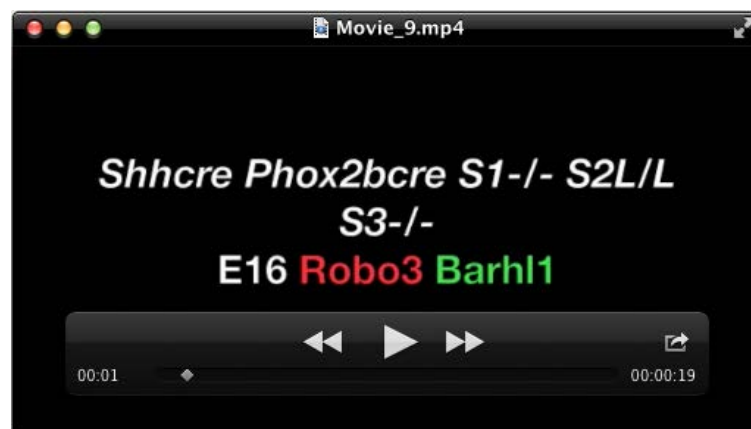
Movie 7

3D movie of the migrating stream of pontine neurons in a *Shh:Cre;S1$^{-/-}$;S2$^{L/L}$;S3$^{-/-}$* E16 embryo. Whole-mount immunolabeling for Barhl1 (Green) and Robo3 (Red) and 3DISCO clearing.

Movie 8

3D movie of the migrating stream of pontine neurons in a *Phox2b:Cre;S1$^{-/-}$;S2$^{L/L}$;S3$^{-/-}$* E16 embryo. Whole-mount immunolabeling for Barhl1 (Green) and Robo3 (Red) and 3DISCO clearing.

Movie 9

3D movie of the migrating stream of pontine neurons in a *Shh:Cre;Phox2b:Cre;S1$^{-/-}$;S2$^{L/L}$;S3$^{-/-}$* E16 embryo. Whole-mount immunolabeling for Barhl1 (Green) and Robo3 (Red) and 3DISCO clearing.

Movie 10

3D stack of optical sections through the inferior olive of a wild type E13 embryo. Whole-mount immunolabeling for Foxp2.

Movie 11

3D stack of optical sections through the inferior olive of a *Robo1⁻/⁻;Robo2⁻/⁻* E13 embryo.

Whole-mount immunolabeling for Foxp2. Note that some Foxp2 neurons are found within the midline.

Movie 12

3D stack of optical sections through the inferior olive of a *Slit1⁻/⁻;Slit2ᐤ/ᐤ;Slit3⁻/⁻* E13 embryo. Whole-mount immunolabeling for Foxp2. Note that some Foxp2 neurons are found within the midline.

Movie 13

3D stack of optical sections through the inferior olive of a *Shh:Cre;S1^{-/-};S2^{L/L};S3^{-/-}* E13 embryo. Whole-mount immunolabeling for Foxp2. Note that a few Foxp2 neurons are found within the midline.